



This is a repository copy of *Lanthanum doped Zn<sub>0.5</sub>Co<sub>0.5</sub>LaxFe<sub>2</sub> spinel ferrites synthesized via co-precipitation route to evaluate structural, vibrational, electrical, optical, dielectric, and thermoelectric properties.*

White Rose Research Online URL for this paper:  
<https://eprints.whiterose.ac.uk/172921/>

Version: Accepted Version

---

**Article:**

Aslam, A., Rehman, A.U., Amin, N. et al. (8 more authors) (2021) Lanthanum doped Zn<sub>0.5</sub>Co<sub>0.5</sub>LaxFe<sub>2</sub> spinel ferrites synthesized via co-precipitation route to evaluate structural, vibrational, electrical, optical, dielectric, and thermoelectric properties. *Journal of Physics and Chemistry of Solids*, 154. 110080. ISSN 0022-3697

<https://doi.org/10.1016/j.jpcs.2021.110080>

---

© 2021 Elsevier. This is an author produced version of a paper subsequently published in *Journal of Physics and Chemistry of Solids*. Uploaded in accordance with the publisher's self-archiving policy. Article available under the terms of the CC-BY-NC-ND licence (<https://creativecommons.org/licenses/by-nc-nd/4.0/>).

**Reuse**

This article is distributed under the terms of the Creative Commons Attribution-NonCommercial-NoDerivs (CC BY-NC-ND) licence. This licence only allows you to download this work and share it with others as long as you credit the authors, but you can't change the article in any way or use it commercially. More information and the full terms of the licence here: <https://creativecommons.org/licenses/>

**Takedown**

If you consider content in White Rose Research Online to be in breach of UK law, please notify us by emailing [eprints@whiterose.ac.uk](mailto:eprints@whiterose.ac.uk) including the URL of the record and the reason for the withdrawal request.



[eprints@whiterose.ac.uk](mailto:eprints@whiterose.ac.uk)  
<https://eprints.whiterose.ac.uk/>

# Lanthanum doped $Zn_{0.5}Co_{0.5}La_xFe_{2-x}O_4$ spinel ferrites synthesized *via* co-precipitation route to evaluate structural, vibrational, electrical, optical, dielectric, and thermoelectric properties

Asma Aslam<sup>a</sup>, Atta Ur Rehman<sup>a</sup>, Nasir Amin<sup>a</sup>, M. Ajaz un Nabi<sup>a</sup>, Qurat ul ain Abdullah<sup>a</sup>, N. A. Morley<sup>b</sup>, Muhammad Imran Arshad<sup>a\*</sup>, Hafiz T Ali<sup>c</sup>, Mohammad Yusuf<sup>d</sup>, Zartashia Latif<sup>a</sup>, Kiran Mehmood<sup>a</sup>

<sup>a</sup>*Department of Physics, Government College University, Faisalabad, 38000, Pakistan.*

<sup>b</sup>*Department of Materials Science and Engineering, The University of Sheffield, UK, S1 3JD.*

<sup>c</sup>*Department of Mechanical Engineering, College of Engineering, Taif University, P.O. Box 1109, Taif 21944, Saudi Arabia*

<sup>d</sup>*Department of Clinical Pharmacy, College of Pharmacy, Taif University, P.O. Box 1109, Taif 21944, Saudi Arabia.*

\*Corresponding Author: [miarshadgcuf@gmail.com](mailto:miarshadgcuf@gmail.com)

## Abstract

Lanthanum doped  $Zn_{0.5}Co_{0.5}La_xFe_{2-x}O_4$  spinel ferrites were synthesized *via* the co-precipitation technique. To characterize the structural, vibrational, electro-optical, dielectric, and thermoelectric properties, the following characterization techniques X-ray diffraction (XRD), Fourier transformation infrared (FTIR) and Raman spectroscopy, I-V measurement analysis, UV-vis spectroscopy, LCR meter, Seebeck analysis, and Energy dispersive X-ray analysis (EDX) were used. The XRD patterns showed nano-crystalline single-phase structure formation. Moreover, the lattice constant increased from  $8.3909 \pm 0.0042 \text{ \AA}$  to  $8.3994 \pm 0.0042 \text{ \AA}$ , and the crystallite size reduced from 33.6 to 17.5 nm with increasing  $La^{3+}$  cations. The bond angles showed stronger  $A-A$  and  $A-B$  interactions and weak  $B-B$  interactions with the addition of  $La^{3+}$ . FTIR spectra showed the existence of the M-O stretching band and functional group study. The resistivity, optical band gap, and activation energy had maximum values at  $x = 0.1$ . At room temperature (RT), the dielectric parameters were recorded between the range of 8 Hz to 8 MHz. The Seebeck voltage coefficient was obtained for the as-prepared nano-ferrites to determine the charge carrier type. The EDX spectra showed a compositional distribution of the elements in all the samples.

**Keywords:** co-precipitation method; structural; electro-optical; dielectric;

## 1 Introduction

The nano-level methodology initiated by Professor Feynman has witnessed drastic changes in the understanding of materials research over several decades [1]. Magnetic nanomaterials have a prominent place in established material science because of their importance in various technological areas [2, 3]. Numerous magnetic materials have demonstrated their versatility in a variety of applications, from heat transport fluid to inductive heat production [4, 5], from magnetic data recorders to microwave devices [6-8], and from medical diagnostics to disease treatments [9-11]. Nano ferrites are a primary material within the category of magnetic materials consisting of mixed composition of transition metal cations and iron oxide. Nano ferrites are divided into three main areas based on their crystal matrix, i.e., hexagonal, spinel, and garnet nano ferrites. Spinel ferrites are the most promising of these three types of ferrites because of their stable and straightforward lattice structure, versatile cation distribution, suitable properties, easy preparation, and accommodation of dopant ions [12-18]. The cation distribution between the two-spinel ferrite intrinsic lattice sites is subjected to ions balance. Typically, the metal ions prefer site energies that characterize normal spinel or inverse spinel or mixed spinel matrix behaviour [19]. The different properties of spinel ferrites are improved by various means such as stoichiometric proportions, preparation method, inclusion of metal divalent or trivalent cations in the spinel lattice, etc. The methods of preparation often affect the shape and the crystallite size of nano ferrites, resulting in structural change [17, 18]. The integration of dopant ions into a lattice, either divalent/trivalent or magnetic/nonmagnetic, results in a drastic change in structural and other properties by cations distribution. In this context, the selection of dopants is a prerequisite for achieving the desired improvement in the pristine spinel ferrites. In addition to transitional dopants like  $Zn^{2+}$ ,  $Cu^{2+}$ ,  $Cd^{2+}$ ,  $Co^{2+}$ , rare earth metals cation dopants like  $La^{3+}$ ,  $Ce^{3+}$ ,  $Dy^{3+}$ ,  $Sm^{3+}$ ,  $Eu^{3+}$ ,  $Ho^{3+}$ ,  $Gd^{3+}$ , etc can be added in small amounts, resulting in a radical change in the spinel ferrites [20, 21].

Several researchers studied  $La^{3+}$  doped Zn [22], and Co [23, 24] nano ferrites. Bahhar *et al.* examined the impact of  $La^{3+}$  on various properties of Zn nano ferrites and described that crystallite size obtained from XRD analysis decreased with  $La^{3+}$  concentration [22]. Hemeda *et al.* synthesized  $CoLa_xFe_{2-x}O_4$  by employing the ceramic route and claimed that the secondary phase of  $LaFeO_3$  formed as a concentration of  $La^{3+}$  increased, and resistivity decreased as the dopant concentration increased. This decreasing trend in resistivity suggests that the conduction process for as-prepared samples is due to the hopping of charge carriers

[23].  $CoLa_xFe_{2-x}O_4$  was developed using the co-precipitation technique. The impact of  $La^{3+}$  on electrical and dielectric parameters of  $Co^{2+}$  ferrites were investigated. The dielectric loss decreased with  $La^{3+}$  concentration, and at  $x = 0.2$  had a minimum value. The DC electrical resistivity of pure cobalt ferrites was  $6.465 \times 10^5 \Omega \text{ cm}$  and increased with the dopant content [24].

There are many goal-oriented methods of preparation, like the microemulsion process [25], self-igniting auto combustion route [26, 27], co-precipitation method [28-30], and the hydrothermal method [31]. There is no literature at present on the  $La^{3+}$  doped Co-Zn spinel ferrite samples produced using the co-precipitation method. The co-precipitation method was used due to the high yield, not requiring the use of organic solvents, high product purity, and ease of reproducibility. It is also easier, more convenient to control the particle size and a low-cost route of preparation [32-34]. The aim of our work is the optimization of the structural, vibrational, electro-optical, dielectric, and thermoelectric properties in  $Zn_{0.5}Co_{0.5}La_xFe_{2-x}O_4$  ( $0.0 \leq x \leq 0.1$  with a step interval of 0.025) spinel ferrite samples at low sintering temperature prepared by the co-precipitation route.

Mugutkar *et al.* synthesized Zn-Co (ZC) nano ferrites with the substitution of  $Gd^{3+}$  and reported lattice impactions and strain were enhanced in the crystals [35]. The crystalline size ( $D$ ) increased with the substitution of  $Nd^{3+}$  in Zn-Co ferrites [36]. Almessiere *et al.* reported that pure Zn-Co ferrite has a maximum value optical bandgap, which increased with the addition of  $Nd^{3+}$  cations [37]. The activation energy and electrical resistivity were enhanced *via* substitution of  $Pr^{3+}$  in Zn-Co nano ferrites [38]. The changed in the Raman modes confirm the destruction in lattice matrix in  $Ho^{3+}$  doped ZC ferrites and optical bandgap was increased with the addition of dopant [39]. Hence, as compared to other rare-earth doped ZC nano ferrites  $La^{3+}$  substituted Zn-Co ferrites have a small crystalline size and high electrical resistivity.

## 2 Experimental detail

### 2.1 Material and Method

$Zn_{0.5}Co_{0.5}La_xFe_{2-x}O_4$  ( $0.0 \leq x \leq 0.1$  with a step interval of 0.025) powder was prepared using a co-precipitation route. For this purpose, highly pure AR grade chemicals Co  $(NO_3)_2 \cdot 6H_2O$  (98.5%), La  $(NO_3)_3 \cdot 6H_2O$  (99.99%), Zn  $(NO_3)_2 \cdot 6H_2O$  (98%), and Fe  $(NO_3)_3 \cdot 9H_2O$  (99.95%), were used according to stoichiometry calculations. The precursors of the series were mixed in de-ionized water to achieve a solution of 100 ml for each nitrate separately, which was then put in the magnetic stirrer at  $80^\circ C$ . Sodium hydroxide was added

drop by drop in this solution to achieve pH 12. The hydroxides of the metals used were produced at this pH value and the size of the particles and their nucleation rate were also controlled. To obtain precipitates, ferrite samples were placed in the preheated water bath at 80°C for 12 hours. These precipitates were collected using filter paper and dehydrated in the oven at 80°C for 24 hours. Then the as-prepared samples were ground in the ceramic mortar to obtain fine powder. The as-prepared samples were then sintered at 1023 K in a muffle furnace, and characterized by different techniques. The schematic step by step version of the co-precipitation route is represented in Fig. 1.

## 2.2 Characterization Techniques Used

To record the diffraction peaks, the X-ray diffractometer (Bruker D8 Advance) with  $\lambda = 0.154$  nm and a  $2\theta$  range of  $20^\circ - 60^\circ$  was used. FTIR spectroscopy (Perkin) was employed to confirm absorption band spectra within the range of wave number 3000 to  $400\text{ cm}^{-1}$ . Raman spectra were recorded using the LABRAM-HR commercial spectrometer. The DC resistivity was determined by the I-V measurement technique (Keithley Electrometer Model 2400). UV-Visible Double Beam Spectrophotometer (UV-DS) Model Lambda 25, Perkin Elmer was used to measure the energy bandgap ( $E_g$ ). IM3533 series LCR Meter used for the dielectric measurements. The thermoelectric properties were measured as a function of temperature for all the samples by a Keithley Electrometer.

## 3 Results and Discussion

### 3.1 Structural Analysis

Diffraction investigations were performed using X-rays, to confirm the phase developments and crystallinity of  $Zn_{0.5}Co_{0.5}La_xFe_{2-x}O_4$  (where  $x = 0.0, 0.025, 0.05, 0.075, 0.1$  and  $0.125$ ) nano ferrite powder. X-ray diffractogram for  $La^{3+}$  doped Zn-Co ( $La^{3+}$  doped ZC) nano ferrite samples fabricated *via* the co-precipitation route are depicted in Fig. 2, after sintering at 1023 K.

The diffraction peak positions appeared at  $30.03^\circ, 35.40^\circ, 37.02^\circ, 42.96^\circ, 53.35^\circ,$  and  $56.87^\circ$ , which concur with (220), (311), (222), (400), (422), and (511) planes respectively of  $La^{3+}$  doped ZC (JCPDS#77-0013). Thus all the samples, were FCC (Face centered cubic) single-phase spinel structures belonging to the space group;  $Fd-3m$  [27, 40]. No extra peaks related to  $La^{3+}$  or byproducts were observed for samples  $x = 0.0$  to  $0.075$ . But at a higher concentration of  $La^{3+}$ , very small intensity peaks were observed between the two peaks (222) and (400), and another peak was found between the peaks (422) and (511) for the samples  $x = 0.1$  and  $x = 0.125$  corresponds to  $LaFeO_3$  (JCPDS#75-0541). The highest intensity peak (311)

was used to calculate the values of the different lattice parameters. The calculated values of the crystallite size ( $D$ ) [41] are given in Table 1. It can be seen that the values of “ $D$ ” for all the prepared samples decreased from 33.6 to 17.5 nm, with increasing  $\text{La}^{3+}$  doping. This may be because of the difference in ionic radii between  $\text{La}^{3+}$  (1.06 Å) and  $\text{Fe}^{3+}$  (0.67 Å) cations, This decrease in crystallite size is due to the bond formation energy of  $\text{La}^{3+}\text{-O}^{2-}$  and  $\text{Fe}^{3+}\text{-O}^{2-}$ , since the bond energy of  $\text{La-O}$  is greater than  $\text{Fe-O}$  which signpost that the more energy is required for the replacement of  $\text{La}^{3+}$  at the octahedral site in Zn-Co nano ferrite. Due to this substitute  $\text{La}^{3+}$  cations enter at interstitial site which suppresses the crystallization of Zn-Co ferrites. [42, 43]. So, it is more difficult to substitute  $\text{La}^{3+}$  cations as compared to  $\text{Fe}^{3+}$  cations on the spinel matrix. The value of the experimental lattice constant ( $a_{\text{exp}}$ ) [44] for the (311) plane is reported in Table 1. The experimental lattice constant ( $a_{\text{exp}}$ ) increased linearly with the raising  $\text{La}^{3+}$  doping for the as-prepared samples, which is because of the variation between the ionic radii of both  $\text{La}^{3+}$  cations and  $\text{Fe}^{3+}$  cations. The small variation in the lattice constant is due to the replacement of  $\text{La}^{3+}$  (1.06 Å) greater cationic radii ions than  $\text{Fe}^{3+}$  (0.67 Å) ions at the octahedral site. Consequently, a small extension was observed in Zn-Co nano ferrites. The dislocation line density ( $\delta$ ) increased with decreasing the crystallite size ( $D$ ) [45]. The dislocation line density ( $\delta$ ) of the nano ferrite samples increased from  $8.86 \times 10^{-4}$  to  $31.8 \times 10^{-4} \text{ nm}^{-2}$  with increasing the  $\text{La}^{3+}$  concentration. The volume of the unit cell increased linearly from  $590.78 \text{ \AA}^3$  to  $592.58 \text{ \AA}^3$  as the  $\text{La}^{3+}$  concentration increased from  $x = 0.0$  to  $0.125$ . Tetrahedral ( $A$ -) site hopping length  $H_A$  and octahedral ( $B$ -) site hopping length  $H_B$  were calculated [46]. It is observed from Table 1 that the magnetic ions distance increased with  $\text{La}^{3+}$  doping. This behaviour of  $A$ - site hopping length “ $H_A$ ” and  $B$ - site hopping length “ $H_B$ ” is analogous with the behaviour of experimental lattice constant ( $a_{\text{exp}}$ ). It may be due to the difference in ionic radii of constituent cations [47].

The X-ray density ( $\rho_x$ ) increased from  $5.34 \pm 0.00535$  to  $5.56 \pm 0.00557 \text{ g/cm}^3$  with the addition of the  $\text{La}^{3+}$  content (Table 2), as the increase in molecular weight overtakes, the increase in the volume of unit cell [48]. The bulk density ( $\rho_B$ ) increased from 3.29 to 4.95  $\text{g/cm}^3$  with the addition of  $\text{La}^{3+}$  cations (Table 2). The relative density ( $\rho_R$ ) decreased from 162.57 % to 112.43 % as  $\text{La}^{3+}$  doping increased from  $x = 0.0$  to  $x = 0.125$ . The values of porosity ( $P$ ) percentage for the nano ferrite powder decreased from 38.38 % to 11.05 %, with increasing  $\text{La}^{3+}$  concentrations from  $x = 0.0$  to  $0.125$  (Table 2). The variation among the X-ray density ( $\rho_x$ ), bulk density ( $\rho_B$ ), relative density ( $\rho_R$ ) and porosity percentage versus dopant  $\text{La}^{3+}$  are shown in Fig. 3(a). Both densities were observed to increase with increment of  $\text{La}^{3+}$  cations.

This increase in densities may be due to different ionic radii of  $\text{La}^{3+}$  (1.05 Å) as that of  $\text{Fe}^{3+}$  (0.645 Å) ions, while the porosity decreased with the addition of  $\text{La}^{3+}$ .

The packing factor ( $p$ ) [49], strain ( $\epsilon$ ) [50], and specific surface area ( $S$ ) [47] of all the samples were calculated. It was observed in Table 2 the packing factor ( $p$ ) decreased with  $\text{La}^{3+}$  concentration. This may be due to the difference in the cationic radii of rare earth  $\text{La}^{3+}$  and  $\text{Fe}^{3+}$  cations [51]. The strain value ( $\epsilon$ ) increased with dopant concentration increase. The specific surface area ( $S$ ) was also enhanced with the addition of  $\text{La}^{3+}$  cations. The variation of strain ( $\epsilon$ ), packing factor ( $p$ ), and specific surface area ( $S$ ) with  $\text{La}^{3+}$  concentrations are given in Fig. 3(b). Because of the formation of polaron (electron-phonon interactions), the charge carriers are not free in spinel ferrites but are highly localized in their d-shells. A slight polaron defect is produced as a result of the displacement of neighboring atoms or ions when a charge carrier is trapped at a given lattice site [52]. It can be noted from Table 2 that the calculated polaron radius ( $\gamma_p$ ) increased with  $\text{La}^{3+}$  doping. This suggests that the electric charge carriers required more energy from one cationic lattice site to another. The high activation energy values calculated from electrical measurements also endorse the increase in polaron radius [52]. The plot of polaron radius ( $\gamma_p$ ), hopping length  $H_A$  and  $H_B$  versus  $\text{La}^{3+}$  concentrations are shown in Fig. 3(c).

Several researchers have used this method to determine the cation distribution [53-55]. The  $\text{La}^{3+}$  substituted Zn-Co nano ferrites formula proposed for all the samples can be represented as  $(\text{Zn}_{0.5}^{2+}\text{Co}_{0.05}^{2+}\text{Fe}_{0.45}^{3+}) [\text{Co}_{0.45}^{2+}\text{Fe}_{1.55-x}^{3+}\text{La}_x^{3+}] \text{O}_4^{2-}$ . This formula is based on hypotheses; i) The sum cationic distribution at tetrahedral site is one and at octahedral site is two. ii) The spinel ferrite net charge must be zero. Therefore, to create an electrically neutral structure, the number of positive charges must equal the number of negative charges in the compound. There are eight  $A$ - sites and 16  $B$ - sites occupied by the divalent and trivalent cations in the spinel matrix. The  $\text{Zn}^{2+}$  cations occupy  $A$ -sites rather than  $B$ -sites [51].  $\text{Co}^{2+}$  and  $\text{Fe}^{3+}$  occupy both  $A$ - and  $B$ - sites [56].  $\text{La}^{3+}$  cations replace  $\text{Fe}^{3+}$  cations from  $B$ -site [51].

In addition to the experimentally observed values of the lattice parameters, the average cations radius  $r_A$  at  $A$ - site, and  $r_B$  at  $B$ - site were determined [57]. It is clear from Table 3 and Fig. 4 that  $r_A$  remains the same, but  $r_B$  increased with a dopant concentration. This variation in  $r_B$  is due to the extension of  $B$ -site on substitution with greater radii  $\text{La}^{3+}$  (1.06 Å) cations [51]. The values of the theoretical lattice constant ( $a_{\text{th}}$ ) increase with increasing  $\text{La}^{3+}$  (Table 3). The difference between the  $a_{\text{th}}$  and  $a_{\text{exp}}$  values is due to the approximation used for the  $a_{\text{th}}$  measurements that consider an ideal unit cell of spinel structure with cations and anions as rigid

spheres arranged regularly [58]. The variation of  $\text{La}^{3+}$  concentration versus crystallite size ( $D$ ), experimental ( $a_{\text{exp}}$ ), and theoretical ( $a_{\text{th}}$ ) lattice constant are given in Fig. 5. The oxygen position parameter ( $U$ ) was calculated using the theoretical and experimental parameters [58]. It is clear from Table 3 and Fig. 6 that the values of “ $U$ ” decreased with dopant concentration. It is noted that the calculated values of “ $U$ ” are higher than an ideal value ( $U_{\text{ideal}} = 0.375\text{\AA}$ ), which is for a perfect closed packing structure, but actually, the lattice is slightly deformed, due to small movements of anions towards tetrahedral ( $A$ -) sites [59]. For a perfectly closed packed structure, the tolerance factor values ( $T$ ) is one [60]. It can be observed from Table 3 and Fig. 6 that the calculated values of “ $T$ ” decreased with an increasing  $\text{La}^{3+}$  concentration from  $x = 0.0$  to  $x = 0.125$ . The metal-oxygen bond length “ $R_A$ ” on  $A$ - site, and metal-oxygen bond length “ $R_B$ ” on  $B$ - site both depend on oxygen position parameters and experimental lattice constant [61]. The calculated values of  $R_A$  and  $R_B$  are reported in Table 3. It can be seen from Fig. 4 that  $R_A$  decreased and  $R_B$  increased with  $\text{La}^{3+}$  doping. The calculated values shared tetrahedral site edge length ( $R_x$ ), shared octahedral site edge length ( $R_x'$ ), and unshared octahedral site edge length ( $R_x''$ ) [51] are listed in Table 3 and vary in accordance with the lattice parameter.

Magnetic interaction strength plays a vital role and can be measured from the angle and distance between the ions [49]. The interionic distance between the ions, i.e., cation-anion ( $\text{Me} - \text{O}$ ) distance ( $p$ ,  $q$ ,  $r$ , and  $s$ ) and cation-cation ( $\text{Me} - \text{Me}$ ) distance ( $b$ ,  $c$ ,  $d$ ,  $e$ , and  $f$ ) were calculated [49]. The calculated values of the interionic distance between the ions are in Table 4 and depicted in Fig. 7. It was found that these values depend on the  $\text{La}^{3+}$  concentration and were used to find the bond angles values  $\theta_1$ ,  $\theta_2$ ,  $\theta_3$ ,  $\theta_4$ , and  $\theta_5$  [49]. The determined bond angles are listed in Table 5 and depicted in Fig. 9 and with  $\text{La}^{3+}$  doping, increase in values of  $\theta_1$ ,  $\theta_2$ , and  $\theta_5$  indicate strong  $A-A$  and  $A-B$  interactions, while decreased in the values of  $\theta_3$  and  $\theta_4$  represent weak  $B-B$  interaction. The values of interionic distance and bond angles are graphically represented in Fig. 7.

### 3.2 Functional Group Analysis

The existence of two different vibrating modes corresponding to spinel lattice were detected by the spectroscopy technique FTIR. FTIR spectra for the nano ferrite powders were recorded within the range of  $400\text{-}3000\text{ cm}^{-1}$  are represented in Fig. 8. FTIR spectroscopy is a spectroscopic method to obtain information about the position of the metal ions within the crystal lattice through the occurrence of different vibrational bands in the crystal lattice and also about cation distribution [62]. It can be seen from Fig. 8 that there are two major bands, which are reported in Table 6. The low-frequency absorption band is  $\nu_2$ , and the high-frequency

absorption band is  $\nu_1$ . The lower absorption frequency band for nano ferrite samples varies from 408.03 - 417.17  $\text{cm}^{-1}$  and the upper-frequency band 542.32 - 555.69  $\text{cm}^{-1}$ . The absorption bands, at a lower frequency, corresponds to the octahedral site and the high-frequency absorption bands correspond to the tetrahedral site within the spinel structure of nano ferrites [63].

The variation in positions is basically due to the difference in the bond length and bond strength of these different synthesized materials. The change in wavenumber may be due to the difference in radii of dopant  $\text{La}^{3+}$  (1.032 Å) and  $\text{Fe}^{3+}$  (0.64 Å), which affects  $\text{Fe}^{3+}-\text{O}^{2-}$ . Moreover, the different vibrational bands also occurred in the sample. The bands occurred around 1418  $\text{cm}^{-1}$  because of the stretching vibration of nitrate ions [64], peaks around 1653  $\text{cm}^{-1}$  attributed to the absorption of H-O-H group with bending vibration [65], the doublet peak at 2354  $\text{cm}^{-1}$  is from ambient  $\text{CO}_2$  gas [66].

### 3.3 Raman Analysis

Raman spectrum at RT for  $\text{La}^{3+}$  substituted Zn-Co nano ferrite was recorded within the range of 200-800  $\text{cm}^{-1}$  and is depicted in Fig. 9. It was measured to study the vibrational properties. The spinel structure ferrites belong to  $Fd-3m$  with eight formula units per unit cell. According to space group theory, the following set of optical phonon mode at  $\Gamma$  point of Brillouin zone exist in ferrites, i.e.,  $\Gamma = A_{1g}(R) + E_g(R) + T_{1g} + 3T_{2g}(R) + 2A_{2u} + 2E_u + 5T_{1u}(IR) + 2T_{2u}$  [67]. For the same vibrational mode, the existence of an inversion center in the Centro-symmetrical space group  $Fd-3m$  indicates the mutual exclusion of Raman ( $R$ ) and Infrared ( $IR$ ) activities.  $A_{1g}(R)$ ,  $E_g(R)$ , and  $3T_{2g}(R)$  are the five first active modes detected in the Raman spectra. Notations  $A$ ,  $E$ ,  $T$ , and  $g$  represent one, two, three-dimension representation and symmetry to the center of inversion, respectively. In  $\text{La}^{3+}$  substituted nano ferrite samples (Fig. 9), five active modes are observed along with some additional vibrational modes that do not correspond to any of the active five modes [68, 69]. The presence of such modes corresponds to the dislocation, impurities, and lattice deformation in the lattice defects or crystal structure. However, since the results of XRD spectra show a single-phase structure, then the existence of such bands is considered as another confirmation of the crystal field deformation. Due to variation in polarizability during molecular vibration in the crystal field, which depends on a loss of symmetry, the Raman modes occur [69, 70]. In the spinel cubic structure ferrites, the five active modes corresponding to the motion of oxygen metal ions are reported in Table 7.  $A_{1g}$  is due to the symmetric stretch of  $\text{FeO}_4$  and appears at 635.98-639.94  $\text{cm}^{-1}$ .  $T_{2g}(3)$  is due to symmetric and asymmetric bends of  $\text{O}^{2-}$  to  $\text{Fe}$  and appears at 508.83-

549.18  $\text{cm}^{-1}$ .  $T_{2g}$  (2) seems at 404.95-468.71  $\text{cm}^{-1}$  and is due to an antisymmetric stretching of  $Fe$ , and  $O^{2-}$ .  $E_g$  is symmetric bending of  $O^{2-}$  to  $Fe$ , and observed at 327.46-367.15  $\text{cm}^{-1}$ .  $T_{2g}$  (1) appears at 286.19-314.78  $\text{cm}^{-1}$  and is attributed to the translational motion of  $FeO$  [71, 72]. The broadening that occurs in the peaks is because of the asymmetric response of the crystal field, as seen by vibrating dipoles. Therefore, we assume that it increases the concept of the deformed crystal structure.

### 3.4 Current-Voltage (I-V) measurement analysis

The DC electrical resistivity of  $La^{3+}$  doped ZC nano ferrite samples was determined. The electrical properties of nanomagnetic materials are based on the sintering temperature, cation distribution at different lattice sites, and method of preparation [73]. The transition temperature after which the material's resistivity changes is known as the Curie temperature. The ferromagnetic region is the region below the Curie temperature. The region above the Curie temperature is paramagnetic. It was observed from Fig. 10 that the DC resistivity of all the samples increased as the temperature increased in the ferro region and decreased with increasing temperature in the para region. Samples where the DC resistivity reduces with rising temperature show semiconducting behavior. However, the band theory which describes the conduction process in semiconductor materials is not appropriate for soft ferrites. The polaron hopping mechanism is used to explain conduction in soft ferrites. It was observed in Fig. 11(a-d) that the DC resistivity is a minimum at  $x = 0.05$  for the ferro and para region. It may be due to the presence of  $Fe^{2+}$  ions formed during sintering, as  $La^{3+}$  is added [74]. It was also clear from Fig. 11(a-c) that at  $x = 0.1$  the DC resistivity is a maximum in the ferro and para regions. But above 503 K, the maximum resistivity was observed at  $x = 0.0$  (Fig. 11(d)). This may be due to the increasing disorder in the structure.

Fig. 12 shows the variation of the  $1000/T$  versus  $\log \rho$  of the  $La^{3+}$  doped Zn-Co nano ferrite samples. Two regions are observed in the  $\log \rho$  vs.  $1000/T$  plots. The region below the Curie temperature ( $T_C$ ) corresponds to the low activation energy region (Ferromagnetic region) and the region above Curie temperature ( $T_C$ ) corresponds to the high activation energy region (Paramagnetic region) [73]. The determined value of the " $T_C$ " for  $La^{3+}$  substituted samples is listed in Table 8. It was observed from Fig. 13 that the minimum value of " $T_C$ " was 352 K for  $x = 0.1$ . The activation energy ( $\Delta E$ ) was calculated by taking the slope of  $\log \rho$  vs.  $1000/T$  (Arrhenius plots) using  $\Delta E = 2.303 \times k_B \times 1000 \times slope (eV)$  [57]. The maximum activation energy ( $\Delta E$ ) was  $1.7345 \pm 0.0086$  eV for  $x = 0.1$ , and variation with  $La^{3+}$

concentration is reported in Fig. 13. It can be observed that activation energy ( $\Delta E$ ), which is in good agreement with the DC resistivity trend.

The drift mobility ( $\mu_d$ ) [57] of  $\text{La}^{3+}$  doped ZC nano ferrite samples as a function of temperature, is represented in Fig. 14. The calculated values of drift mobility ( $\mu_d$ ) at 313 K are reported in Table 8 and graphically as a function of  $\text{La}^{3+}$  concentration ( $x$ ) are given in Fig. 13. They have the opposite trend with the DC resistivity because both drift mobility and DC resistivity are inversely related to each other.

### 3.5 UV-vis analysis

The optical band gap in nano ferrites depends on the following factors including dopant concentration, structure parameters, particle size, surficial effects, lattice strains, and impurities [75]. The UV-vis pattern of  $\text{La}^{3+}$  doped ZC ferrite samples is shown in Fig. 15. By employing the Tauc plot, the value of the optical band gap ( $E_g$ ) of the as-prepared was determined. The optical band gaps ( $E_g$ ) for  $x = 0.0$  to  $x = 0.125$  are reported in Table 8. It was clear from Table 8 that the optical band gaps ( $E_g$ ) have a maximum value of 3.63 eV for  $x = 0.1$ .

### 3.6 Dielectric Analysis

Electrical dipoles form by the interaction of the charged di- and trivalent metal ions in the spinel matrix. The chemical composition, sintering temperature, distribution of metal ions among  $A$ - and  $B$ - sites, and methods of preparation are all responsible for the dielectric behaviour of iron oxide [76, 77]. To study the impact of the variation of  $\text{La}^{3+}$  cations, the dielectric constant ( $\epsilon'$ ), dielectric loss ( $\epsilon''$ ), dielectric tangent loss ( $\tan \delta$ ), and ac conductivity ( $\sigma_{ac}$ ) were determined as a function of applied frequency at RT for the La-doped Zn-Co nano ferrite samples. The variation between  $\epsilon'$  and  $\epsilon''$  with the frequency for nano ferrite samples are shown in Fig. 16(a). At high frequency, both  $\epsilon'$  and  $\epsilon''$  indicate variable values. But as the applied frequency is reduced both dielectric constant ( $\epsilon'$ ) and loss ( $\epsilon''$ ) decrease. It can be seen in Fig. 16(a) that an abrupt decrease is observed in dielectric loss ( $\epsilon''$ ) but dielectric constant ( $\epsilon'$ ) does not have a rapid decrease. Various researchers reported the same dielectric response in spinel ferrites and explained it based on the Maxwell Wagner's interfacial polarization theory [78, 79]. The degree of energy dissipation in the materials is known as a dielectric tangent loss ( $\tan \delta$ ) [80]. The variation in  $\tan \delta$  vs frequency for nano ferrite samples is represented in Fig. 16(b) within the frequency range 8 Hz to 8 MHz. It observed in Fig. 16(b) that the value of  $\tan \delta$  is large at low frequency and small at high frequency. This is due to the grains with thinner boundaries that are more efficient at a low frequency as compared to the conducting grains, which cause higher dielectric tangent loss [80]. The variation between  $\text{La}^{3+}$

concentration and tangent loss is given in Fig. 17(a-c). It was observed in Fig. 17(a) at a low frequency that the dielectric tangent loss has minimum values as compared to other concentrations for a high concentration of  $\text{La}^{3+}$  ( $x = 0.1$ ). But in the kHz and MHz frequency ranges sample  $x = 0.1$  has a maximum value of tangent loss Fig. 17(b-c).

The measure of the ability to conduct an electric current in nano ferrite samples is known as ac conductivity ( $\sigma_{ac}$ ) [80]. Fig. 18 indicates the graphical representation of the ac conductivity ( $\sigma_{ac}$ ) as a function of frequency. It is observed in Fig. 18 there are two regions, i.e., low and high-frequency regions. The ac conductivity ( $\sigma_{ac}$ ) increased with applied frequency for both low and high frequency. This phenomenon is characteristics of soft ferrites because the grain boundaries have low conductivity, and the grains are highly conductive[80].

### 3.6 Thermoelectric analysis

Fig. 19 shows the relation between the Seebeck voltage coefficient ( $S$ ) with temperature for  $\text{La}^{3+}$  substituted Zn-Co nano-ferrite samples. The existence of more than one region shows the presence of more than one conduction process [81]. The Seebeck voltage coefficient ( $S$ ) is divided into two groups, the first one of  $x = 0.0-0.05, 0.125$ , while the second is for  $x = 0.075-0.1$ . It observed that the charge carrier's variation between n- and p- types depend on the concentration ( $x$ ) of  $\text{La}^{3+}$  cations. For the first group ( $x = 0.0-0.05, 0.125$ ), it indicates that the conduction process is due to small positive polarons and gives a positive Seebeck voltage coefficient ( $S$ ). In the second group, the conduction process is due to electrons and gives a negative Seebeck voltage coefficient ( $S$ ). The positive values for samples  $x = 0.0-0.05, 0.125$  show p-type materials while negative values for samples  $x = 0.075-0.1$  indicate n-type materials. The power factor (PF) depends on the square of the Seebeck voltage coefficient ( $S^2$ ) and electrical conductivity ( $\sigma = 1/\rho$ ) [82-85]. The values of power factor (PF) calculated using  $\text{PF} = S^2\sigma$  for  $\text{La}^{3+}$  substituted ZC nano-ferrites at 323 K, 423 K, and 523 K and graphically as given in Fig. 20.

### 3.7 Element compositional analysis

The elements within the chemical composition for  $\text{La}^{3+}$  substituted Zn-Co nano-ferrites were studied using energy dispersive X-ray (EDX) analysis. The elemental composition analysis for  $\text{Zn}_{0.5}\text{Co}_{0.5}\text{La}_x\text{Fe}_{2-x}\text{O}_4$  nano-ferrites is listed in Table 9. EDX pattern for  $x = 0.0$  and  $x = 0.025$ , are given in Fig. 21. Zn, Co, Fe and O are the main elements in pure  $\text{Zn}_{0.5}\text{Co}_{0.5}\text{Fe}_2\text{O}_4$  observed and replaced by  $\text{La}^{3+}$  detected in samples  $x = 0.025$  to  $x = 0.125$ . The EDX results indicated that the as-prepared samples did not contain any raw element. It also confirmed that the preparation of the iron oxygen was pure and  $\text{La}^{3+}$  cations doping achieved.

## Conclusions

La<sup>3+</sup> substituted Zn-Co samples were fabricated *via* the co-precipitation route. XRD analysis confirmed the as-prepared ferrites have a single-phase cubic matrix. The doping of La<sup>3+</sup> leads to the increasing experimental lattice constant, and reduction in crystallite size. The X-ray density increased from  $5.34 \pm 0.01$  to  $5.56 \pm 0.01$  g/cm<sup>3</sup> with the addition of La<sup>3+</sup> ions. The average cationic radii and hopping lengths indicate a slight variation with increased dopant cations. The interionic distances were observed to decrease with a rise in dopant concentration. Also, the bond angles  $\theta_1$ ,  $\theta_2$ , and  $\theta_5$  tend to be slightly enhanced, while  $\theta_3$  and  $\theta_4$  were observed to slightly reduce with the addition of La<sup>3+</sup>. Hence, the strength of *A–A* and *A–B* interactions increased, while *B–B* interaction decreased. FTIR spectra confirmed two major absorption bands, a low band (408.03-417.17 cm<sup>-1</sup>) and a high band (542.32-555.69 cm<sup>-1</sup>). However, Raman spectra showed *A*<sub>1g</sub>, *E*<sub>1g</sub>, and *3T*<sub>2g</sub> five active modes and indicate symmetric and anti-symmetric behaviour of the vibrational band position of La<sup>3+</sup> doped ZC nano ferrites. The DC resistivity and activation energies were determined from the electrical conduction process and it was observed that both have the same trend. Hence, drift mobility was found to be a minimum for  $x = 0.1$ . UV-vis analysis showed that the optical bandgap maximum for  $x = 0.1$ . Dielectric tangent loss indicates a momentous decreasing trend for Zn<sub>0.5</sub>Co<sub>0.5</sub>La<sub>0.1</sub>Fe<sub>1.9</sub>O<sub>4</sub> nanoparticles at low frequency. The study of the Seebeck voltage coefficient (*S*) and power factor (PF) imply that the as-prepared nano-ferrites are suitable for thermoelectric applications. The La<sup>3+</sup> doped Zn-Co nano-ferrites were divided into n- and p-types semiconductors. EDX show the spatial distribution of elements as well as stoichiometry in all the samples.

## Acknowledgment

The current research is supported by Taif University Researchers Supporting Project number (TURSP - 2020/293), Taif University, Taif, Saudi Arabia. The author Asma Aslam is also highly grateful to HEC, Pakistan for giving her opportunity of research under IRSIP, PIN: IRSIP 46 PSc.27.

## References

- [1] S. Abbas, M. Anis-ur-Rehman, Association of structural and enhanced transport properties in RE substituted cobalt nanoferrites, *Journal of Alloys and Compounds*, 677 (2016) 143-147.
- [2] D.A. Stirling, *Nanotechnology Applications*, in: *The Nanotechnology Revolution*, Pan Stanford, (2018) 281-434.
- [3] A. Somvanshi, S. Husain, W. Khan, Investigation of structure and physical properties of cobalt doped nano-crystalline neodymium orthoferrite, *Journal of Alloys and Compounds*, 778 (2019) 439-451.
- [4] S.B. Somvanshi, R.V. Kumar, J.S. Kounsalye, T.S. Saraf, K. Jadhav, Investigations of structural, magnetic and induction heating properties of surface functionalized zinc ferrite

nanoparticles for hyperthermia applications, in: AIP Conference Proceedings, AIP Publishing LLC 2115 (2019) 030522.

[5] S.R. Patade, D.D. Andhare, S.B. Somvanshi, P.B. Kharat, S.D. More, K.M. Jadhav, Preparation and characterisations of magnetic nanofluid of zinc ferrite for hyperthermia, *Nanomaterials and Energy*, 9 (2020) 1-6.

[6] M. Babrekar, K. Jadhav, Synthesis and characterization of spray deposited lithium ferrite thin film, *International Research Journal of Science Engineering, Special*, 1 (2017) 73-76.

[7] P.B. Kharat, S. More, S.B. Somvanshi, K. Jadhav, Exploration of thermoacoustics behavior of water based nickel ferrite nanofluids by ultrasonic velocity method, *Journal of Materials Science: Materials in Electronics*, 30 (2019) 6564-6574.

[8] P.B. Kharat, S.B. Somvanshi, J.S. Kounsalye, S.S. Deshmukh, P.P. Khirade, K. Jadhav, Temperature dependent viscosity of cobalt ferrite/ethylene glycol ferrofluids, in: AIP Conference Proceedings, AIP Publishing LLC, 1942 (2018) 050044.

[9] A. Sobczak-Kupiec, J. Venkatesan, A.A. AlAnezi, D. Walczyk, A. Farooqi, D. Malina, S.H. Hosseini, B. Tyliczszak, Magnetic nanomaterials and sensors for biological detection, *Nanomedicine: Nanotechnology, Biology and Medicine*, 12 (2016) 2459-2473.

[10] S.B. Somvanshi, P.B. Kharat, M.V. Khedkar, K. Jadhav, Hydrophobic to hydrophilic surface transformation of nano-scale zinc ferrite via oleic acid coating: magnetic hyperthermia study towards biomedical applications, *Ceramics International*, 46 (2020) 7642-7653.

[11] S.B. Kale, S.B. Somvanshi, M. Sarnaik, S. More, S. Shukla, K. Jadhav, Enhancement in surface area and magnetization of  $\text{CoFe}_2\text{O}_4$  nanoparticles for targeted drug delivery application, in: AIP Conference Proceedings, AIP Publishing LLC, 1953 (2018) 030193.

[12] R. Valenzuela, Novel applications of ferrites, *Physics Research International*, (2012) 591839.

[13] D.S. Mathew, R. S. Juang, An overview of the structure and magnetism of spinel ferrite nanoparticles and their synthesis in microemulsions, *Chemical engineering journal*, 129 (2007) 51-65.

[14] S.B. Somvanshi, M.V. Khedkar, P.B. Kharat, K. Jadhav, Influential diamagnetic magnesium ( $\text{Mg}^{2+}$ ) ion substitution in nano-spinel zinc ferrite ( $\text{ZnFe}_2\text{O}_4$ ): Thermal, structural, spectral, optical and physisorption analysis, *Ceramics International*, 46(7), (2020), 8640-8650.

[15] A.M. Abu-Dief, M.S. Abdelbaky, D. Martínez-Blanco, Z. Amghouz, S. García-Granda, Effect of chromium substitution on the structural and magnetic properties of nanocrystalline zinc ferrite, *Material Chemistry and Physics*, 174 (2016) 164-171.

[16] A.A. Marzouk, A.M. Abu-Dief, A.A. Abdelhamid, Hydrothermal preparation and characterization of  $\text{ZnFe}_2\text{O}_4$  magnetic nanoparticles as an efficient heterogeneous catalyst for the synthesis of multi-substituted imidazoles and study of their anti-inflammatory activity, *Applied Organometallic Chemistry*, 32 (2018) e3794.

[17] W. Mohamed, M. Alzaid, M. SM Abdelbaky, Z. Amghouz, S. García-Granda, A.M. Abu-Dief, Impact of  $\text{Co}^{2+}$  substitution on microstructure and magnetic properties of  $\text{Co}_x\text{Zn}_{1-x}\text{Fe}_2\text{O}_4$  nanoparticles, *Nanomaterials*, 9 (2019) 1602.

[18] W. Mohamed, A.M. Abu-Dief, Impact of rare earth europium ( $\text{RE-Eu}^{3+}$ ) ions substitution on microstructural, optical and magnetic properties of  $\text{CoFe}_{2-x}\text{Eu}_x\text{O}_4$  nanosystems, *Ceramics International*, 46 (2020), 16196-16209.

[19] V. Bharati, S.B. Somvanshi, A.V. Humbe, V. Murumkar, V. Sondur, K. Jadhav, Influence of trivalent Al-Cr co-substitution on the structural, morphological and Mössbauer properties of nickel ferrite nanoparticles, *Journal of Alloys and Compounds*, 821 (2020) 153501.

[20] M.A. Almessiere, Y. Slimani, H. Güngüneş, S. Ali, A. Manikandan, I. Ercan, A. Baykal, A. Trukhanov, Magnetic attributes of  $\text{NiFe}_2\text{O}_4$  nanoparticles: Influence of dysprosium Ions ( $\text{Dy}^{3+}$ ) substitution, *Nanomaterials*, 9 (2019) 820.

- [21] M. Almessiere, Y. Slimani, A. Korkmaz, N. Taskhandi, M. Sertkol, A. Baykal, S.E. Shirsath, İ. Ercan, B. Özçelik, Sonochemical synthesis of  $\text{Eu}^{3+}$  substituted  $\text{CoFe}_2\text{O}_4$  nanoparticles and their structural, optical and magnetic properties, *Ultrasonics sonochemistry*, 58 (2019) 104621.
- [22] S. Bahhar, H. Lemziouka, A. Boutahar, H. Bioud, H. Lassri, E. Hlil, Influence of  $\text{La}^{3+}$  site substitution on the structural, magnetic and magnetocaloric properties of  $\text{ZnFe}_{2-x}\text{La}_x\text{O}_4$  ( $x = 0.00, 0.001, 0.005$  and  $0.01$ ) spinel zinc ferrites, *Chemical Physics Letters*, 716 (2019) 186-191.
- [23] O. Hemeda, A. Henaish, S. Mansour, T. Sharshar, M.A. Hamad, Electrical properties and positron annihilation studies of nano-crystalline  $\text{CoLa}_x\text{Fe}_{2-x}\text{O}_4$  prepared by ceramic method, *Applied Physics A*, 126 (2020) 141.
- [24] P. Kumar, S. Sharma, M. Knobel, M. Singh, Effect of  $\text{La}^{3+}$  doping on the electric, dielectric and magnetic properties of cobalt ferrite processed by co-precipitation technique, *Journal of Alloys and Compounds*, 508 (2010) 115-118.
- [25] N. Tian, H. Huang, Y. He, Y. Guo, T. Zhang, Y. Zhang, Mediator-free direct Z-scheme photocatalytic system:  $\text{BiVO}_4/\text{gC}_3\text{N}_4$  organic-inorganic hybrid photocatalyst with highly efficient visible-light-induced photocatalytic activity, *Dalton Transactions*, 44 (2015) 4297-4307.
- [26] M. Hanif, O. Farooq, U. Rafiq, M. Anis-ur-Rehman, A.U. Haq, Structural, dielectric and electrical properties of Gd substituted Lithium Nano-ferrites prepared by Sol-Gel method, *Nanotechnology*, 31(25), (2020), 255707.
- [27] A.U. Rehman, N. Morley, N. Amin, M.I. Arshad, M.A. un Nabi, K. Mahmood, A. Ali, A. Aslam, A. Bibi, M.Z. Iqbal, Controllable synthesis of  $\text{La}^{3+}$  doped  $\text{Zn}_{0.5}\text{Co}_{0.25}\text{Cu}_{0.25}\text{Fe}_{2-x}\text{La}_x\text{O}_4$  ( $x = 0.0, 0.0125, 0.025, 0.0375, 0.05$ ) nano-ferrites by sol-gel auto-combustion route, *Ceramics International*, 46 (2020) 29297-29308.
- [28] A. Aslam, A. Razzaq, S. Naz, N. Amin, M.I. Arshad, M.A.U. Nabi, A. Nawaz, K. Mahmood, A. Bibi, F. Iqbal, N. Magnetism, Impact of Lanthanum-Doping on the Physical and Electrical Properties of Cobalt Ferrites, *Journal of Superconductivity and Novel Magnetism*, (2021) 1-10.
- [29] I. ALIa, N. Amin, A. REHMAN, M. Akhtar, M. Fatima, K. Mahmood, A. ALIa, G. Mustafa, M. Hasan, A. Bibi, Biostructures, ELECTRICAL AND MAGNETIC PROPERTIES OF  $\text{BaCo}_x\text{Cd}_{2-x}\text{Fe}_{16}\text{O}_{27}$  W-TYPE HEXAFERRITES ( $0 \leq x \leq 0.5$ ), *Digest Journal of Nanomaterials & Biostructures*, 15 (2020) 67-73.
- [30] N. Amin, M. Akhtar, M. Sabir, K. Mahmood, A. ALIa, G. Mustafa, M. Hasan, A. Bibi, M. Iqbal, F. Iqbal, SYNTHESIS, STRUCTURAL AND OPTICAL PROPERTIES OF Zn-SUBSTITUTED Co W-FERRITES BY COPRECIPITATION METHOD, *Journal of Ovonic Research*, 16 (2020) 11-19.
- [31] J. Rodney, S. Deepapriya, P. Annie Vinosha, M. Cyril Robinson, S. Krishnan, S. Martin Britto Dhas, S. Jerome Das, Impact of Synthesis Technique on Lanthanum Doped Copper Oxide Nanocrystals, an Alternative Counter Electrode for Pt-Free Dye-Sensitized Solar Cells, *Journal of Nanoscience and Nanotechnology*, 20 (2020) 4023-4034.
- [32] S. Deepapriya, S.L. Devi, P.A. Vinosha, J.D. Rodney, C.J. Raj, J.E. Jose, S.J. Das, Estimating the ionicity of an inverse spinel ferrite and the cation distribution of La-doped  $\text{NiFe}_2\text{O}_4$  nanocrystals for gas sensing properties, *Applied Physics A*, 125 (2019) 683.
- [33] K. Hussain, N. Amin, M.I. Arshad, Evaluation of structural, optical, dielectric, electrical, and magnetic properties of  $\text{Ce}^{3+}$  doped  $\text{Cu}_{0.5}\text{Cd}_{0.25}\text{Co}_{0.25}\text{Fe}_{2-x}\text{O}_4$  spinel nano-ferrites, *Ceramics International*, 47(3) (2020) 3401-3410.
- [34] M. Alzaid, A. Qasem, E. Shaaban, N. Hadia, Extraction of thickness, linear and nonlinear optical parameters of  $\text{Ge}_{20+x}\text{Se}_{80-x}$  thin films at normal and slightly inclined light for optoelectronic devices, *Optical Materials*, 110 (2020) 110539.

- [35] A.B. Mugutkar, S.K. Gore, R.S. Mane, S.M. Patange, S.S. Jadhav, S.F. Shaikh, A.M. Al-Enizi, A. Nafady, B.M. Thamer, M. Ubaidullah, Compounds, Structural modifications in Co–Zn nanoferrites by Gd substitution triggering to dielectric and gas sensing applications, *Journal of Alloys and Compounds*, 844 (2020) 156178.
- [36] B. Sahanashree, E. Melagiriappa, M. Veena, G. Shankaramurthy, H.M. Somashekarappa, Influence of Neodymium and gamma rays irradiation on structural electrical and magnetic properties of Co-Zn nanoferrites, *Materials Chemistry and Physics*, 214 (2018) 143-153.
- [37] M.A. Almessiere, Unique structural and magnetic traits of Nd<sup>3+</sup> substituted Co–Zn nanoferrites, *Journal of Rare Earth*, 37 (2019) 1108-1115.
- [38] H.M.T. Farid, I. Ahmad, K. Bhatti, I. Ali, S.M. Ramay, A. Mahmood, The effect of praseodymium on Cobalt-Zinc spinel ferrites, *Ceramics International*, 43 (2017) 7253-7260.
- [39] R. A. Pawar, S.M. Patange, Q.Y. Tamboli, V. Ramanathan, S.E. Shirsath, Spectroscopic, elastic and dielectric properties of Ho<sup>3+</sup> substituted Co-Zn ferrites synthesized by sol-gel method, *Ceramics International*, 42 (2016) 16096-16102.
- [40] E. C. Devi, I. Soibam, Effect of Zn doping on the structural, electrical and magnetic properties of MnFe<sub>2</sub>O<sub>4</sub> nanoparticles, *Indian Journal of Physics*, 91 (2017) 861-867.
- [41] B. Vigneshwaran, P. Kuppusami, A. Panda, A. Singh, H. Sreemoolanadhan, Microstructure and optical properties of Ba<sub>0.6</sub>Sr<sub>0.4</sub>TiO<sub>3</sub> thin films prepared by pulsed laser deposition, *Materials Research Express*, 5 (2018) 066420.
- [42] Y. Dasan, B. Guan, M. Zahari, L.K. Chuan, Influence of La<sup>3+</sup> substitution on structure, morphology and magnetic properties of nanocrystalline Ni-Zn ferrite, *PLOS One*, 12 (2017) e0170075.
- [43] R.S. Yadav, I. Kuřitka, J. Vilcakova, J. Havlica, L. Kalina, P. Urbánek, M. Machovsky, D. Skoda, M. Masař, Influence of Gd<sup>3+</sup> substitution on structural, magnetic, dielectric and modulus spectroscopic characteristics of ZnFe<sub>2</sub>O<sub>4</sub> spinel ferrite nanoparticles, *Journal of Materials Science: Materials in Electronics*, 29 (2018) 15878-15893.
- [44] I. Ali, M. Islam, M. Ishaque, H.M. Khan, M.N. Ashiq, M.U. Rana, M. Materials, Structural and magnetic properties of holmium substituted cobalt ferrites synthesized by chemical coprecipitation method, *Journal of Magnetism and Magnetic Materials*, 324 (2012) 3773-3777.
- [45] F. Hamed, T. Ramachandran, V. Kurapati, The effect of induced strains on the optical band gaps in lanthanum-doped zinc ferrite nanocrystalline powders, *Modern Physics Letters B*, 30 (2016) 1650230.
- [46] K. A. Ganure, L.A. Dhale, S.E. Shirsath, K.S. Lohar, O. Polymers, Materials, Morphological Study of Lanthanum-Doped Nano Spinel Ferrite via Normal Micelles Method, *Inorganic and Organometallic Polymers and Materials*, 28 (2018) 1821-1828.
- [47] V. Chaudhari, S.E. Shirsath, M. Mane, R. Kadam, S. Shelke, D.R. Mane, compounds, Crystallographic, magnetic and electrical properties of Ni<sub>0.5</sub>Cu<sub>0.25</sub>Zn<sub>0.25</sub>La<sub>x</sub>Fe<sub>2-x</sub>O<sub>4</sub> nanoparticles fabricated by sol–gel method, *Journal of Alloys and Compound*, 549 (2013) 213-220.
- [48] F. Fontaine, G.E. Christidis, J. Yans, S. Hollanders, A. Hoffman, N. Fagel, Characterization and origin of two Fe-rich bentonites from Westerwald (Germany), *Applied Clay Science*, 187 (2020) 105444.
- [49] P. Thakur, R. Sharma, V. Sharma, P. Barman, M. Kumar, D. Barman, S. Katyay, P. Sharma, M. Materials, Gd<sup>3+</sup> doped Mn-Zn soft ferrite nanoparticles: Superparamagnetism and its correlation with other physical properties, *Journal of Magnetism and Magnetic Materials*, 432 (2017) 208-217.
- [50] K. Hussain, A. Bibi, F. Jabeen, N. Amin, K. Mahmood, A. Ali, M.Z. Iqbal, M.J.P.B.C.M. Arshad, Study of structural, optical, electrical and magnetic properties of Cu<sup>2+</sup> doped Zn<sub>0.4</sub>Co<sub>0.6-x</sub>Ce<sub>0.1</sub>Fe<sub>1.9</sub>O<sub>4</sub> spinel ferrites, *Physica B: Condensed Matter*, 584 (2020) 412078.

- [51] P. Thakur, R. Sharma, M. Kumar, S. Katyay, N. Negi, N. Thakur, V. Sharma, P. Sharma, Superparamagnetic La doped Mn–Zn nano ferrites: dependence on dopant content and crystallite size, *Materials Research Express*, 3 (2016) 075001.
- [52] H. Anwar, A. Maqsood, Enhancement of electrical and magnetic properties of Cd<sup>2+</sup> doped Mn–Zn soft nanoferrites prepared by the sol–gel autocombustion method, *Journal of Magnetism and Magnetic Materials*, 333 (2013) 46-52.
- [53] R. M. Kershi, Compounds, Rare-earth ions as a key influencer on the magnetic, spectroscopic and elastic properties of Er<sub>γ</sub>Zn<sub>0.2</sub>Co<sub>0.8</sub>Fe<sub>2-γ</sub>O<sub>4</sub> nanoparticles, *Journal of Alloys and Compounds*, (2020) 158114.
- [54] B. P. Rao, B. Dhanalakshmi, S. Ramesh, P.S. Rao, M. Materials, Cation distribution of Ni-Zn-Mn ferrite nanoparticles, *Journal of Magnetism and Magnetic Materials*, 456 (2018) 444-450.
- [55] C. A.P. Gómez, C.A.B. Meneses, A.J.M.S. Matute, E. B, Structural parameters and cation distributions in solid state synthesized Ni-Zn ferrites, *Materials Science and Engineering: B*, 236 (2018) 48-55.
- [56] D. Mane, D. Birajdar, S. Patil, S.E. Shirsath, R.H. Kadam, technology, Redistribution of cations and enhancement in magnetic properties of sol–gel synthesized Cu<sub>0.7-x</sub>Co<sub>x</sub>Zn<sub>0.3</sub>Fe<sub>2</sub>O<sub>4</sub> (0 ≤ x ≤ 0.5), *Journal of Sol-Gel Science and Technology*, 58 (2011) 70-79.
- [57] K. Mohammed, A. Al-Rawas, A. Gismelseed, A. Sellai, H. Widatallah, A. Yousif, M. Elzain, M. Shongwe, Infrared and structural studies of Mg<sub>1-x</sub>Zn<sub>x</sub>Fe<sub>2</sub>O<sub>4</sub> ferrites, *Physica B: Condensed Matter*, 407 (2012) 795-804.
- [58] H. Zaki, S. Al-Heniti, T. Elmosalami, compounds, Structural, magnetic and dielectric studies of copper substituted nano-crystalline spinel magnesium zinc ferrite, *Journal of Alloys and Compounds*, 633 (2015) 104-114.
- [59] K. Sun, Z. Lan, Z. Yu, Z. Xu, X. Jiang, Z. Wang, Z. Liu, M. Luo, Temperature and frequency characteristics of low-loss MnZn ferrite in a wide temperature range, in, *American Institute of Physics*, 109 (2011), 106103.
- [60] R. Sharma, S. Singhal, Structural, magnetic and electrical properties of zinc doped nickel ferrite and their application in photo catalytic degradation of methylene blue, *Physica B: Condensed Matter*, 414 (2013) 83-90.
- [61] A. Nairan, M. Khan, U. Khan, M. Iqbal, S. Riaz, S. Naseem, Temperature-dependent magnetic response of antiferromagnetic doping in cobalt ferrite nanostructures, *Nanomaterials*, 6 (2016) 73.
- [62] R. Sharma, P. Thakur, P. Sharma, V. Sharma, Ferrimagnetic Ni<sup>2+</sup> doped Mg-Zn spinel ferrite nanoparticles for high density information storage, *Journal of Alloys and Comounds*, 704 (2017) 7-17.
- [63] R. Vemuri, G. Raju, M.G. Kiran, M. Prasad, E. Rajesh, G.P. Kumar, N. Murali, Effect on structural and magnetic properties of Mg<sup>2+</sup> substituted cobalt nano ferrite, *Results in Physics*, 12 (2019) 947-952.
- [64] N. K. Hejazy, T.M. Hammad, A. Sciences, Optical, Structural and Magnetic Properties of Copper-doped Iron Ferrite Synthesized by a Sol-Gel Method, *Palestinian Journal of Technology and Applied Science*, 2 (2019) 82-90.
- [65] R. S. Sari, A.R. Hakim, Bonding analysis of magnetic nanoparticles (MNPS) zinc ferrite (ZnFe<sub>2</sub>O<sub>4</sub>) encapsulated with silica (SiO<sub>2</sub>), in: *IOP Conference Series: Earth and Environmental Science*, IOP Publishing, 382 (2019) 012019.
- [66] H. Kumar, J.P. Singh, R. Srivastava, P. Negi, H. Agrawal, K. Asokan, FTIR and electrical study of dysprosium doped cobalt ferrite nanoparticles, *Journal of Nanoscience*, (2014) 862415.

- [67] A. Kumar, P. Sharma, D. Varshney, Structural, vibrational and dielectric study of Ni doped spinel Co ferrites:  $\text{Co}_{1-x}\text{Ni}_x\text{Fe}_2\text{O}_4$  ( $x = 0.0, 0.5, 1.0$ ), *Ceramics International*, 40 (2014) 12855-12860.
- [68] R. Waldron, Infrared spectra of ferrites, *Physical Review*, 99 (1955) 1727.
- [69] P. Graves, C. Johnston, J.J. Campaniello, Raman scattering in spinel structure ferrites, *Materials Research Bulletin*, 23 (1988) 1651-1660.
- [70] M. Abdellatif, G. Abdelrasoul, M. Salerno, I. Liakos, A. Scarpellini, S. Marras, A.J.C. Diaspro, S.A. Physicochemical, E. Aspects, Fractal analysis of inter-particle interaction forces in gold nanoparticle aggregates, *Colloids and Surfaces A: Physicochemical and Engineering Aspects*, 497 (2016) 225-232.
- [71] O. N. Shebanova, P. Lazor, Raman spectroscopic study of magnetite ( $\text{FeFe}_2\text{O}_4$ ): a new assignment for the vibrational spectrum, *Journal of Solid State Chemistry*, 174 (2003) 424-430.
- [72] K. Mohit, V.R. Gupta, N. Gupta, S.K. Rout, Structural and microwave characterization of  $\text{Ni}_{0.2}\text{Co}_x\text{Zn}_{0.8-x}\text{Fe}_2\text{O}_4$  for antenna applications, *Ceramics International*, 40 (2014) 1575-1586.
- [73] M. Raghasudha, D. Ravinder, P. Veerasomaiah, Electrical resistivity studies of Cr doped Mg nano-ferrites, *Materials Discovery*, 2 (2015) 50-54.
- [74] K. K Rama, K. K Vijaya, R. Dachehalli, chemistry, Structural and electrical conductivity studies in nickel-zinc ferrite, *Advances in Materials physics and chemistry*, 2 (2012) 23241.
- [75] M. Z. Shoushtari, A. Emami, S.E.M. Ghahfarokhi, A study of the doped zinc-ferrite nanoparticles with bismuth, *Materials Research Express*, 5 (2018) 075024.
- [76] C. Ramana, Y. Kolekar, K. Kamala Bharathi, B. Sinha, K. Ghosh, Correlation between structural, magnetic, and dielectric properties of manganese substituted cobalt ferrite, *Journal of Applied Physics*, 114 (2013) 183907.
- [77] R. Pandit, K. Sharma, P. Kaur, R. Kumar, Physics, Cation distribution controlled dielectric, electrical and magnetic behavior of  $\text{In}^{3+}$  substituted cobalt ferrites synthesized via solid-state reaction technique, *Materials Chemistry and Physics*, 148 (2014) 988-999.
- [78] R. Islam, M. Hakim, M. Rahman, H.N. Das, M.J.J.o.a. Mamun, compounds, Study of the structural, magnetic and electrical properties of Gd-substituted Mn-Zn mixed ferrites, *Journal of Alloys and Compounds*, 559 (2013) 174-180.
- [79] N. Gupta, P. Jain, R. Rana, S. Shrivastava, Current development in synthesis and characterization of nickel ferrite nanoparticle, *Materials Today: Proceedings*, 4 (2017) 342-349.
- [80] Y. Köseoğlu, M. Bay, M. Tan, A. Baykal, H. Sözeri, R. Topkaya, N. Akdoğan, Magnetic and dielectric properties of  $\text{Mn}_{0.2}\text{Ni}_{0.8}\text{Fe}_2\text{O}_4$  nanoparticles synthesized by PEG-assisted hydrothermal method, *Journal of Nanoparticle Research*, 13 (2011) 2235-2244.
- [81] S. Solyman, Transport properties of La-doped Mn-Zn ferrite, *Ceramics International*, 32 (2006) 755-760.
- [82] S. B. Mary, A.L. Rajesh, Influence of trivalent lanthanides substitution on the thermoelectric properties of nanostructured  $\text{Ca}_{1-x}\text{Ln}_{3+x}\text{MnO}_{3-\delta}$  ( $\text{Ln}^{3+} = \text{Sm, Ce, La}$ ;  $x = 0, 0.1$ ), *Journal of Materials Science: Materials in Electronics*, (2020) 1-9.
- [83] L. H. Abdel Rahman, A.M. Abu-Dief, R.M. El-Khatib, S.M. Abdel-Fatah, A. Adam, E.M.M. Ibrahim, Sonochemical synthesis, structural inspection and semiconductor behavior of three new nano sized Cu (II), Co (II) and Ni (II) chelates based on tri-dentate NOO imine ligand as precursors for metal oxides, *Applied Organometallic Chemistry*, 32 (2018) e4174.
- [84] A. Elshafaie, L.H. Abdel-Rahman, A.M. Abu-Dief, S.K. Hamdan, A. Ahmed, E.M.M. Ibrahim, Electric, thermoelectric and magnetic properties of Nickel (II) Imine Nanocomplexes, *Nano*, 13 (2018) 1850074.
- [85] E. Ibrahim, L.H. Abdel-Rahman, A.M. Abu-Dief, A. Elshafaie, S.K. Hamdan, A.M. Ahmed, Electric, thermoelectric and magnetic characterization of  $\gamma\text{-Fe}_2\text{O}_3$  and  $\text{Co}_3\text{O}_4$

nanoparticles synthesized by facile thermal decomposition of metal-Schiff base complexes, Materials Research Bulletin, 99 (2018) 103-108.

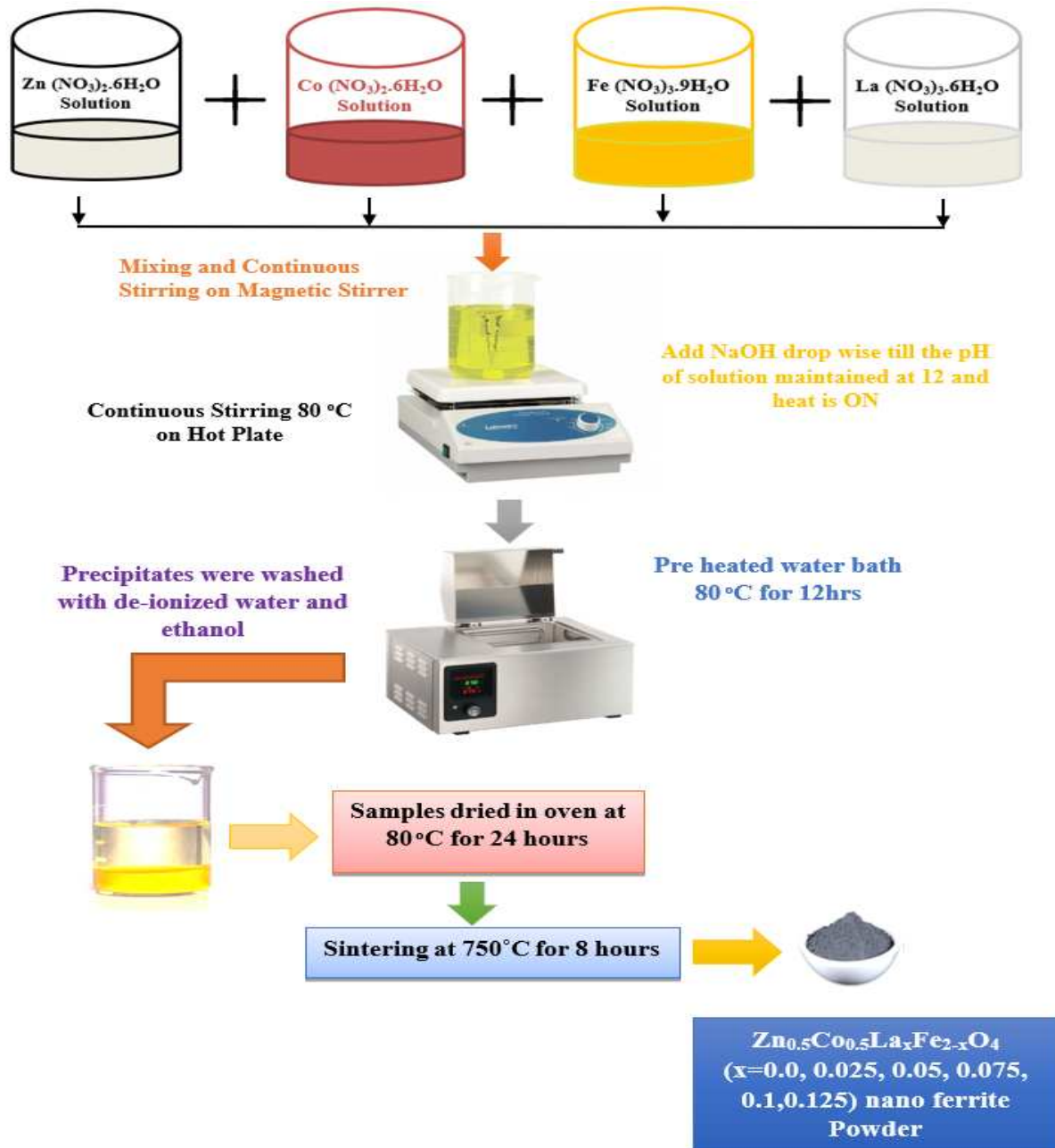


Fig. 1. Schematic diagram of the co-precipitation route for all the samples

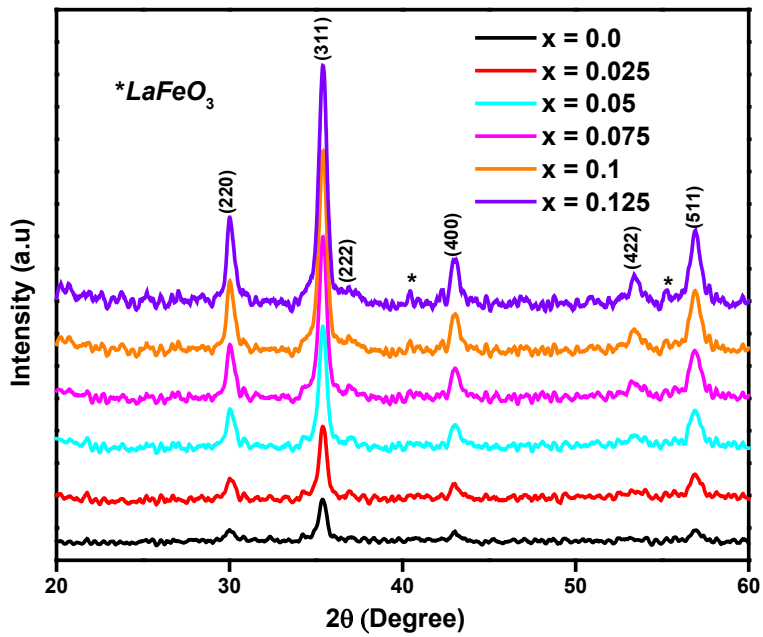
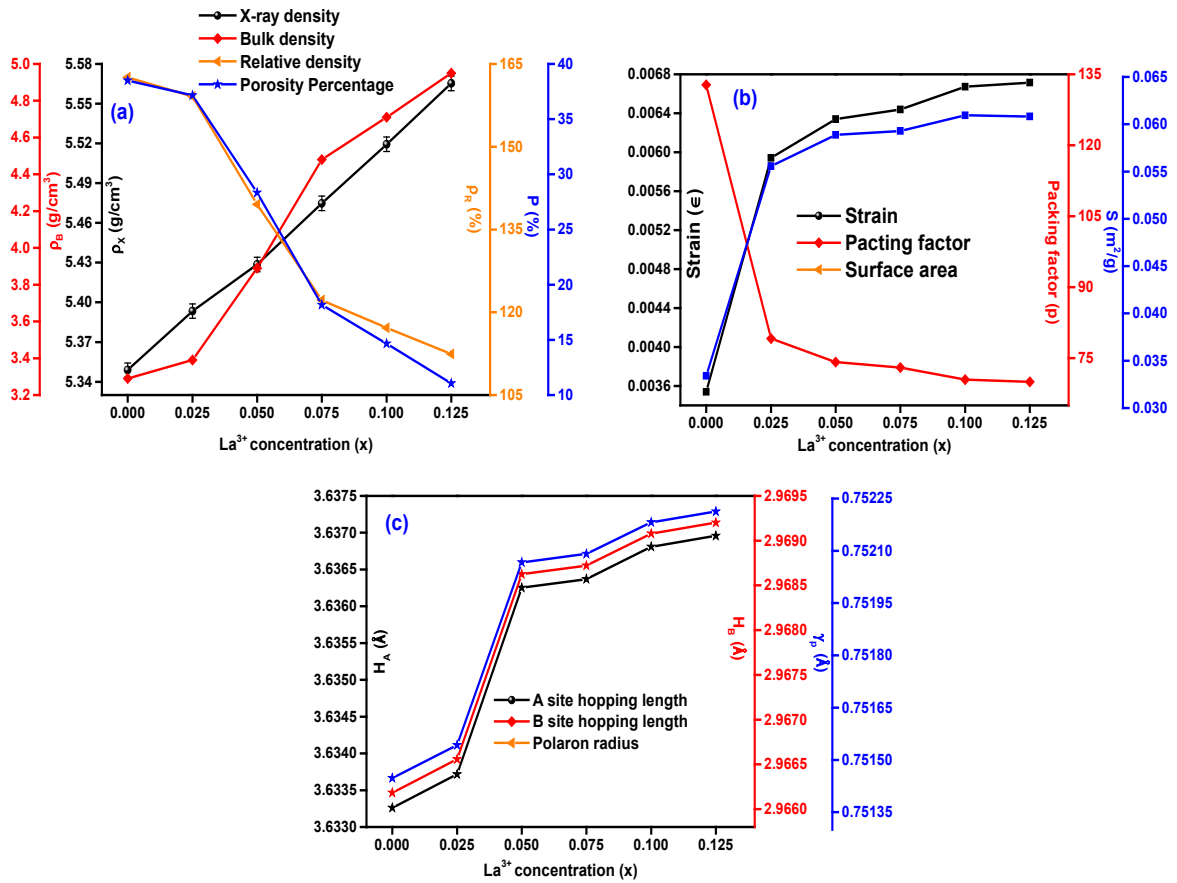
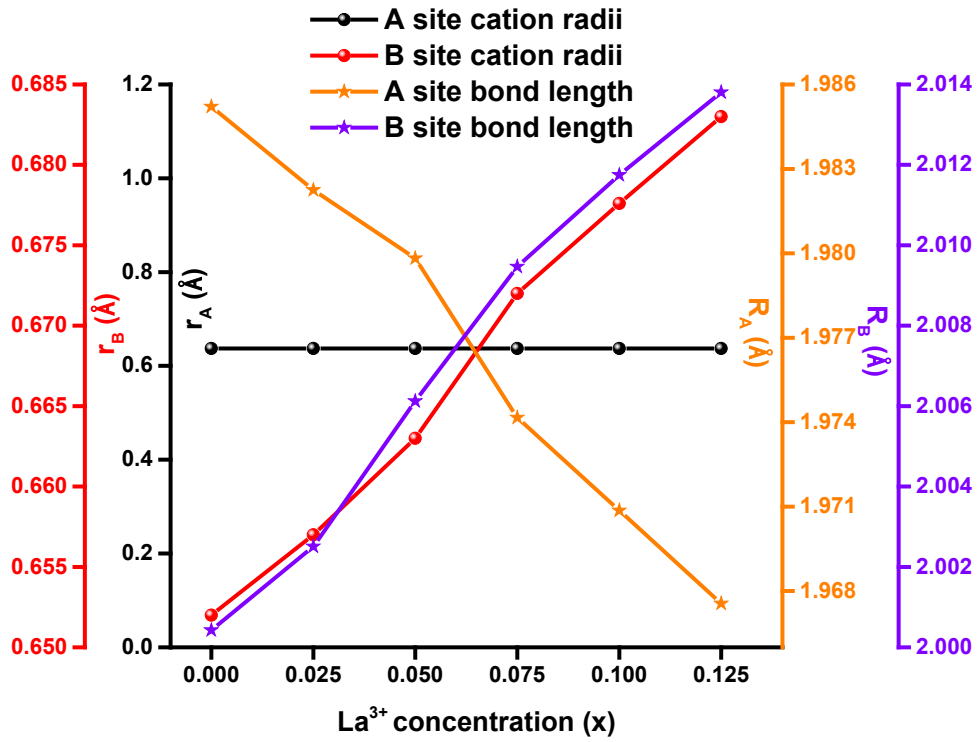


Fig. 2. XRD spectrum of La<sup>3+</sup> doped Zn-Co nano ferrite powder



**Fig. 3.**  $\text{La}^{3+}$  concentration *versus* (a) X-ray, bulk, relative densities, and porosity percentage (b) strain, packing factor, and specific surface area (c) polaron radius, hopping length at *A* and *B* site



**Fig. 4.** A plot of  $\text{La}^{3+}$  concentration vs. cationic radii and bond lengths

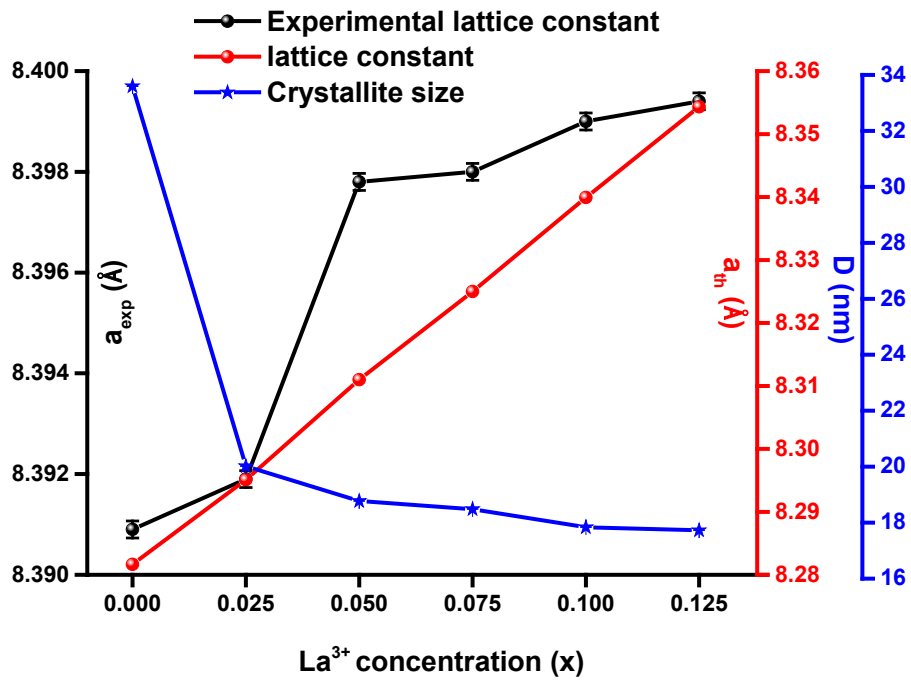


Fig. 5. A plot of La<sup>3+</sup> concentration vs. crystallite size, experimental and theoretical lattice constants

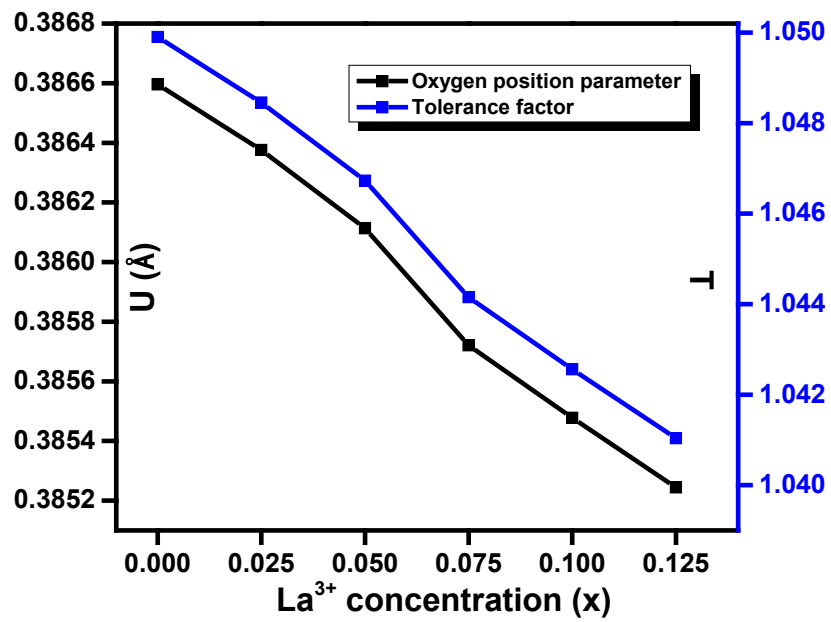


Fig. 6. A plot of La<sup>3+</sup> vs. oxygen position parameter and tolerance factor

### A-B Interaction

$x = 0.0$

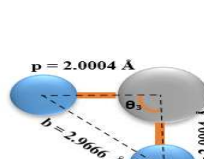


$\theta_1 = 121.57^\circ$

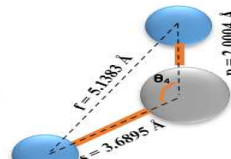


$\theta_2 = 137.71^\circ$

### B-B Interaction

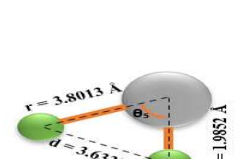


$\theta_3 = 95.71^\circ$



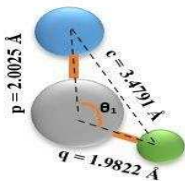
$\theta_4 = 126.53^\circ$

### A-A Interaction

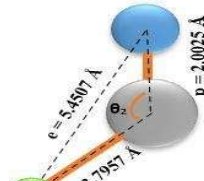


$\theta_5 = 69.88^\circ$

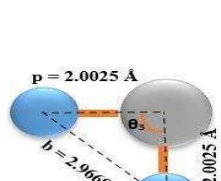
$x = 0.025$



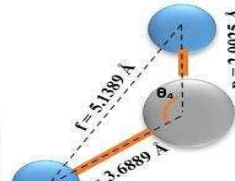
$\theta_1 = 121.64^\circ$



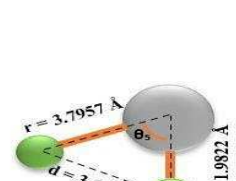
$\theta_2 = 137.97^\circ$



$\theta_3 = 95.60^\circ$

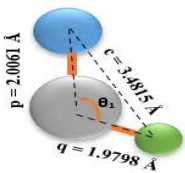


$\theta_4 = 126.51^\circ$

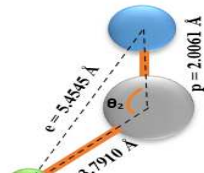


$\theta_5 = 70.05^\circ$

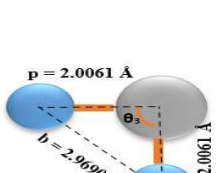
$x = 0.05$



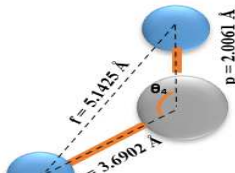
$\theta_1 = 121.72^\circ$



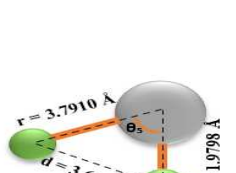
$\theta_2 = 138.28^\circ$



$\theta_3 = 95.46^\circ$



$\theta_4 = 126.48^\circ$



$\theta_5 = 70.26^\circ$

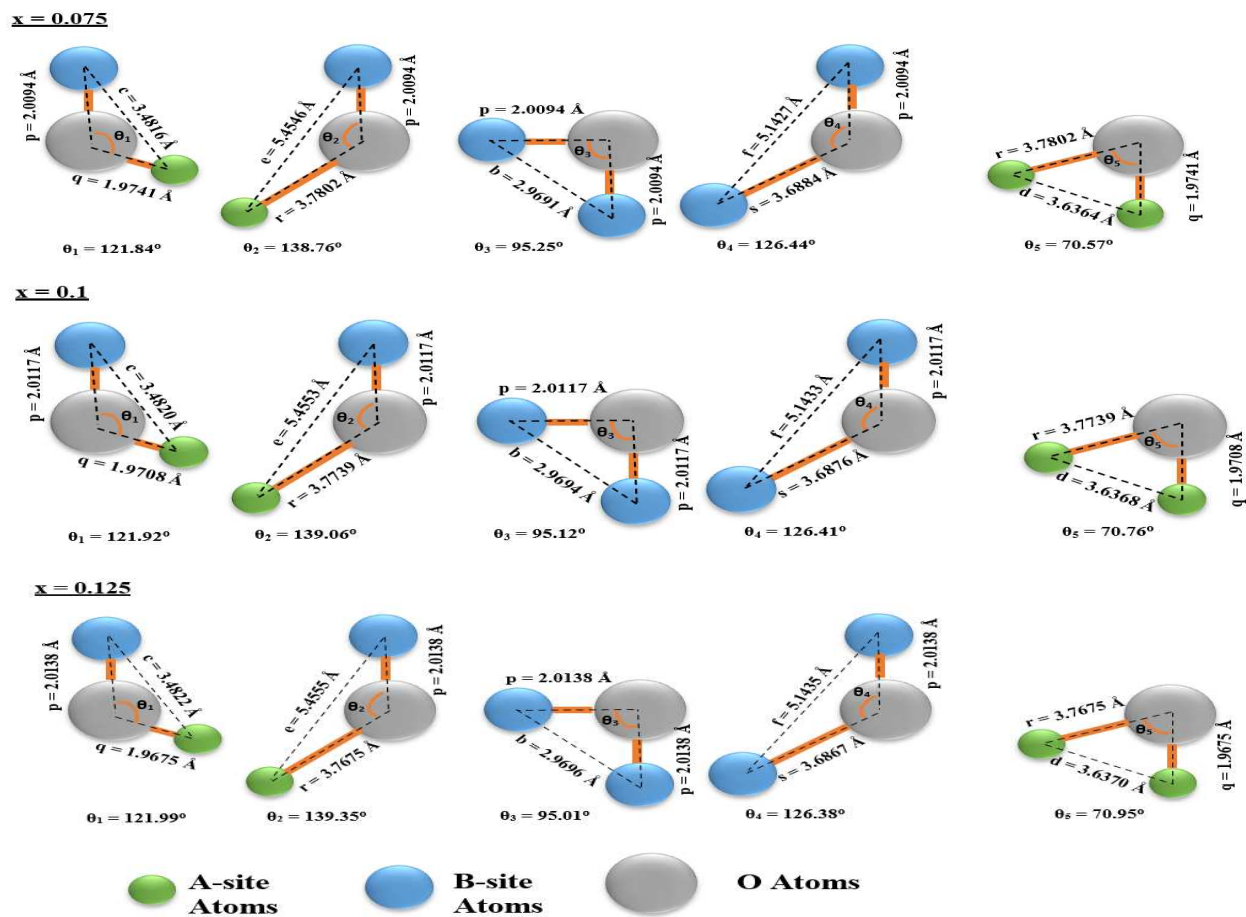


Fig. 7. The relation between interionic distance and bond angles

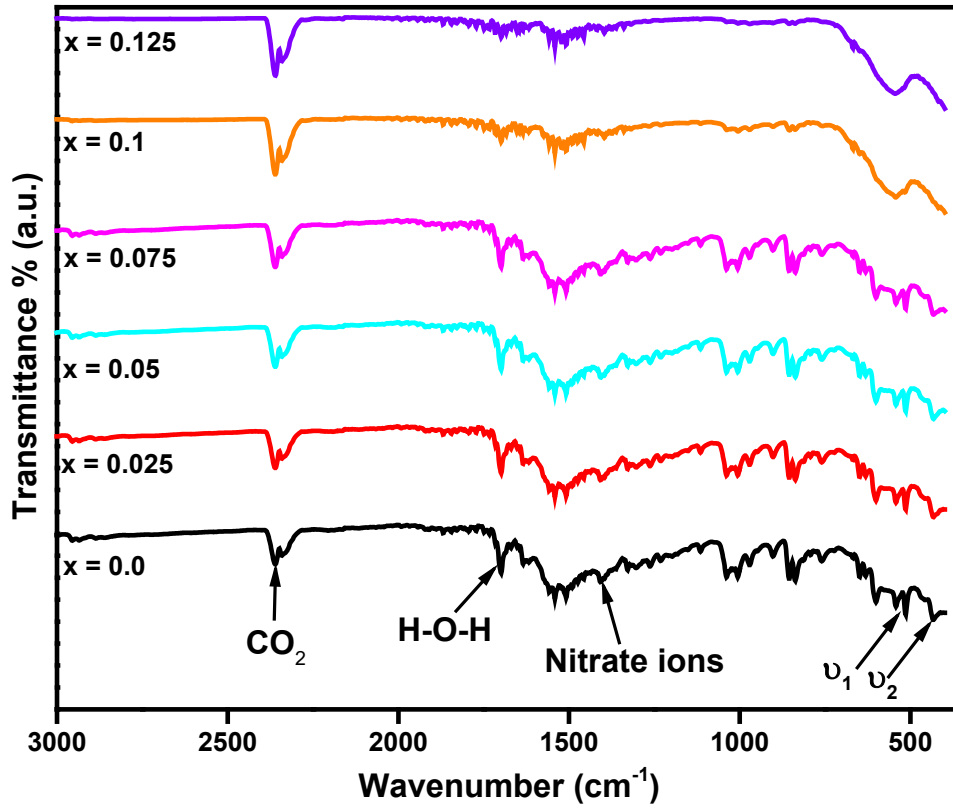


Fig. 8. La<sup>3+</sup> doped ZC nano ferrite samples FTIR spectra

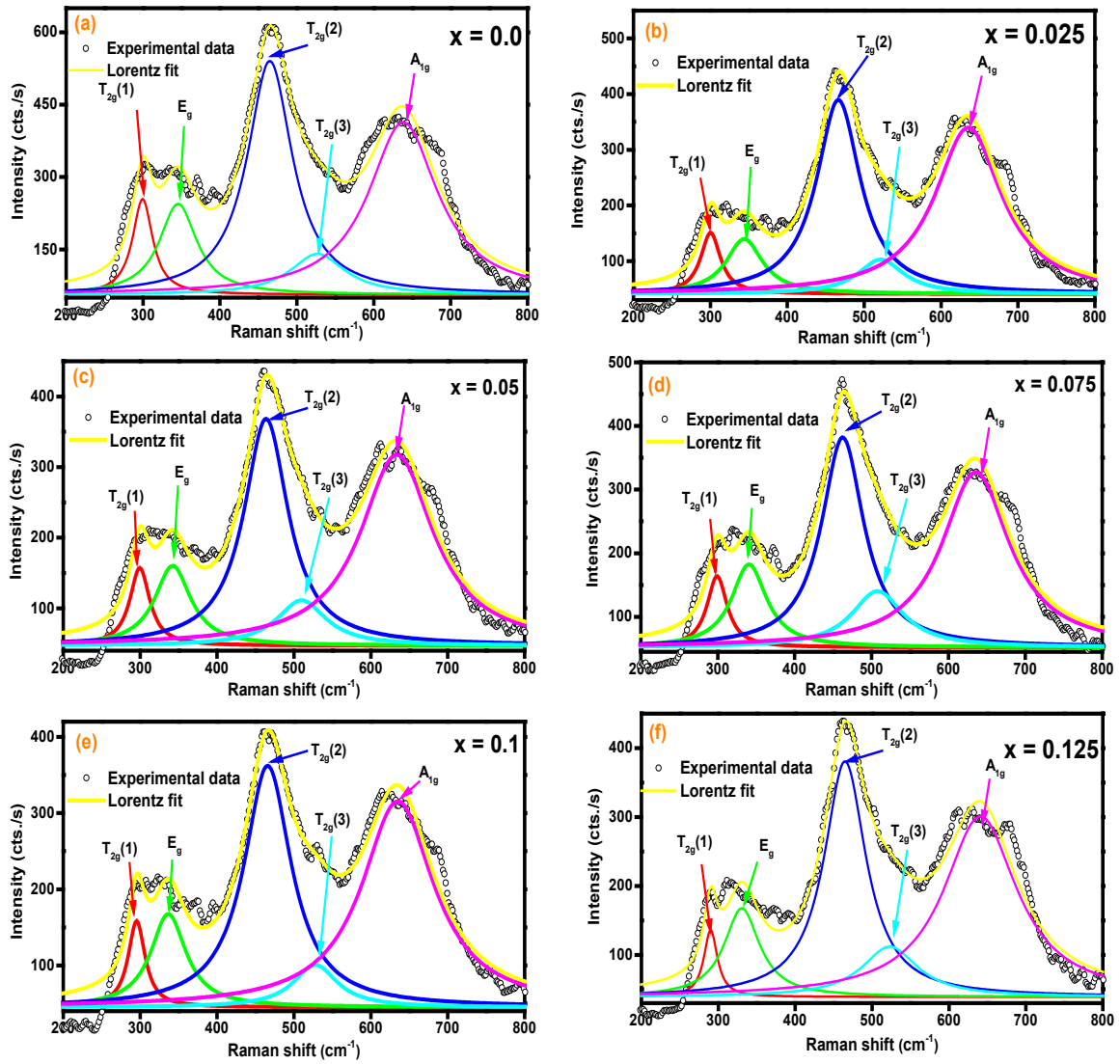


Fig. 9(a-f). Raman spectra of nano ferrite samples at room temperature

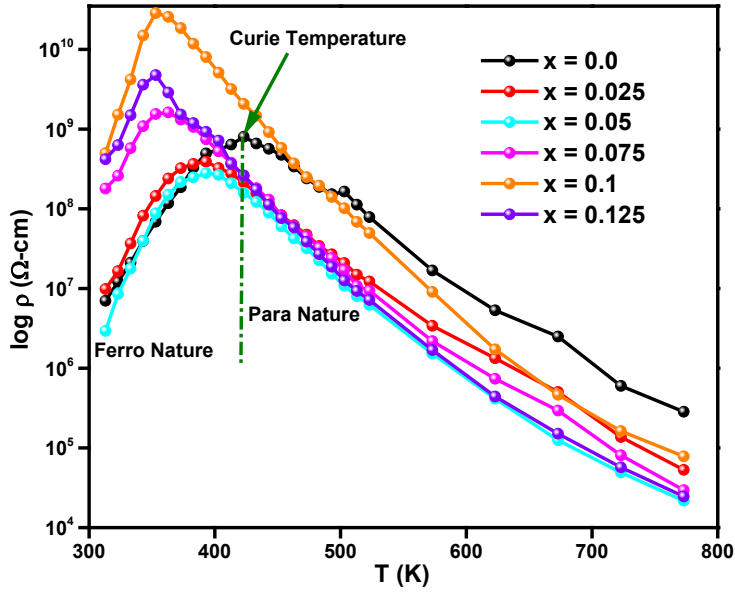


Fig. 10. Temperature vs.  $\log \rho$  for  $\text{La}^{3+}$  doped ZC samples

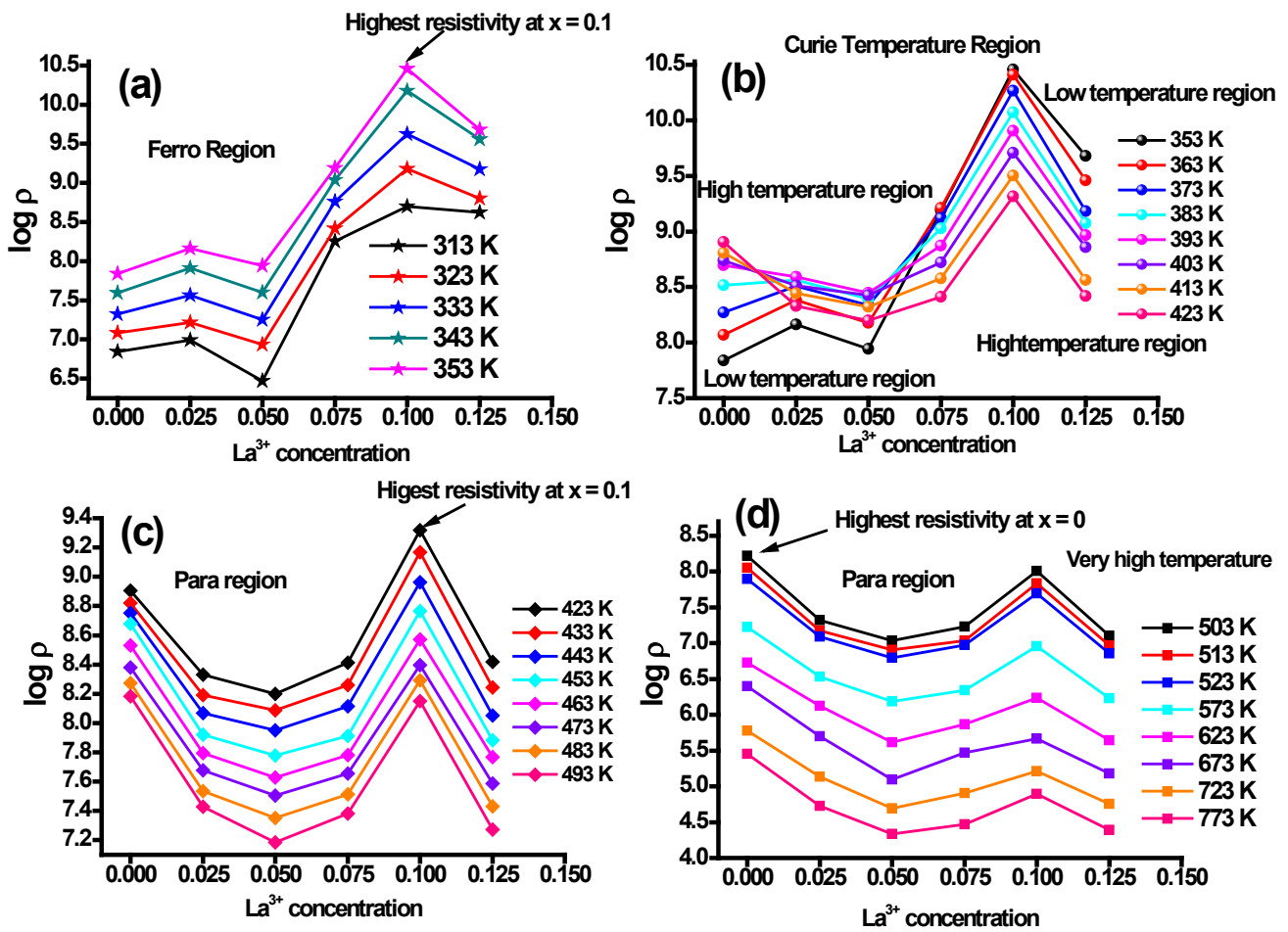


Fig. 11. Plots of  $\text{La}^{3+}$  concentrations vs. resistivity in ferro and para regions

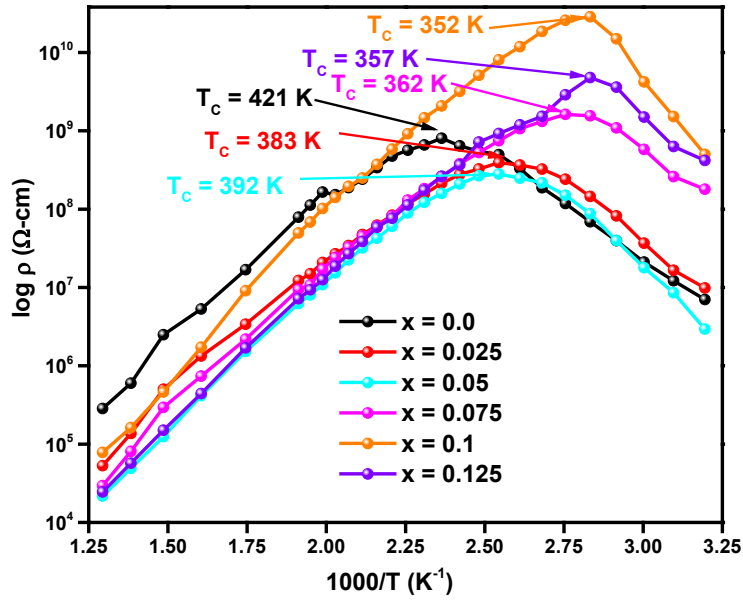


Fig. 12.  $1000/T$  vs.  $\log \rho$  of  $\text{La}^{3+}$  doped Zn-Co nano ferrite samples

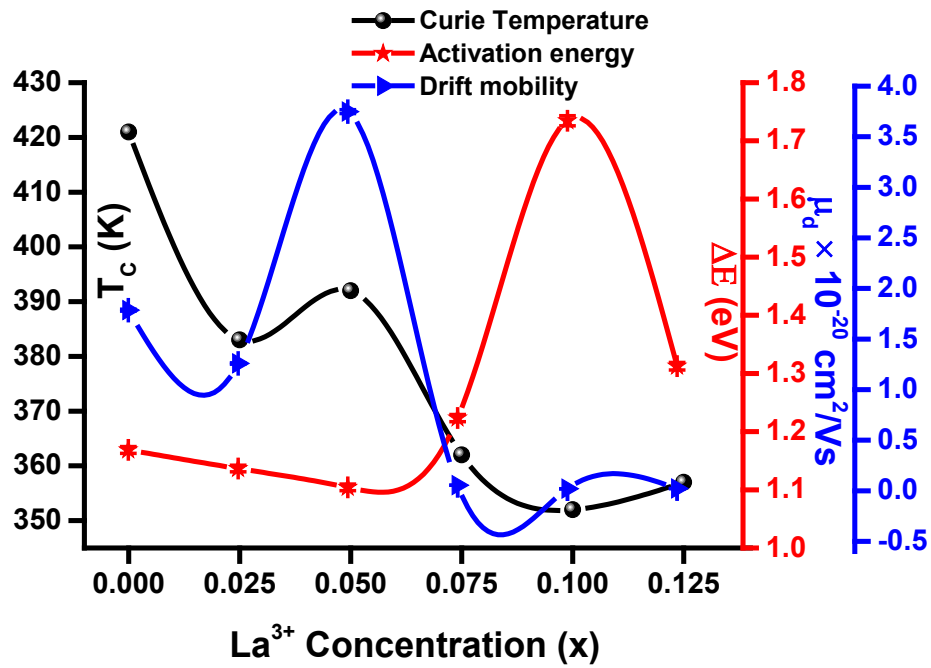


Fig. 13.  $\text{La}^{3+}$  vs. Curie temperature, activation energy, and drift mobility

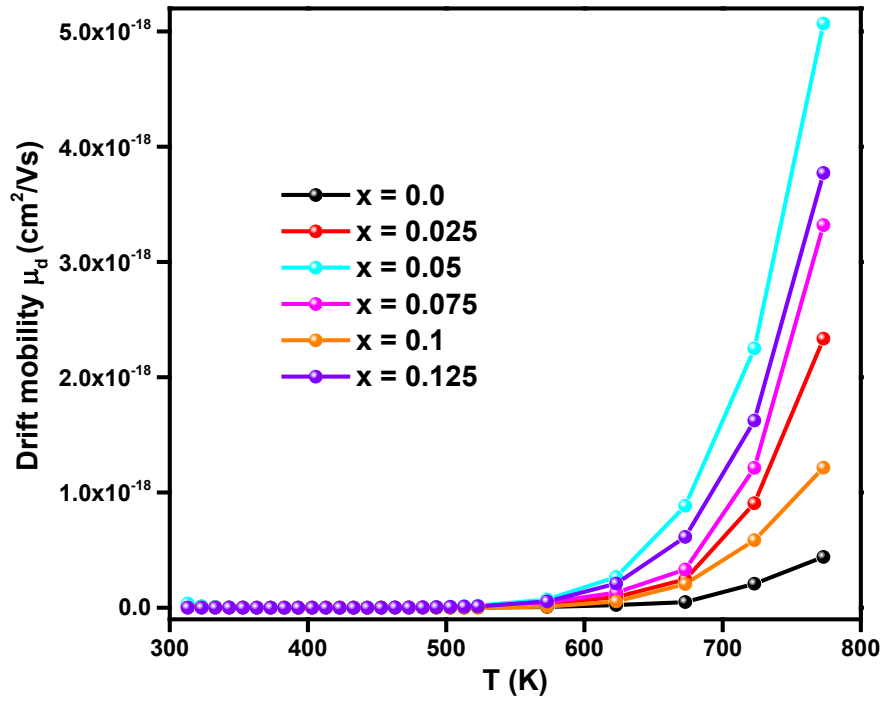


Fig. 14. Temperature vs. drift mobility of  $\text{La}^{3+}$  doped ZC nano-ferrites

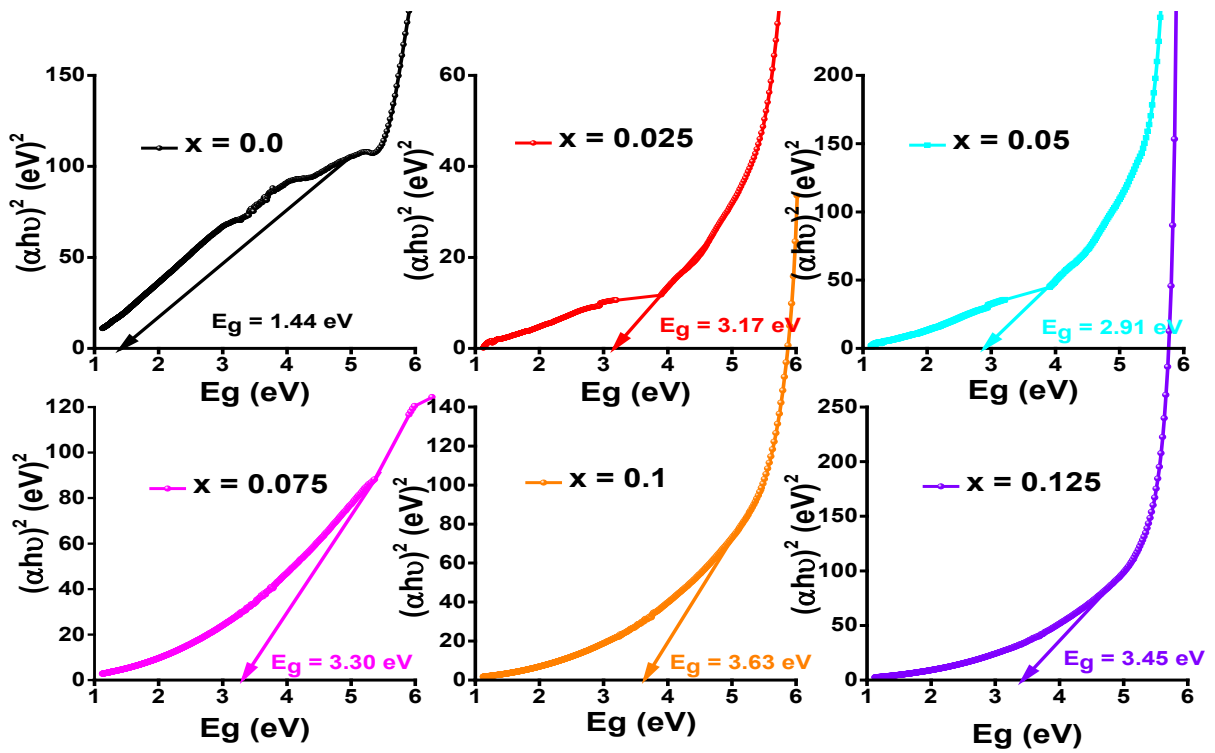


Fig. 15. Tauc plot for  $\text{La}^{3+}$  doped ZC ferrites

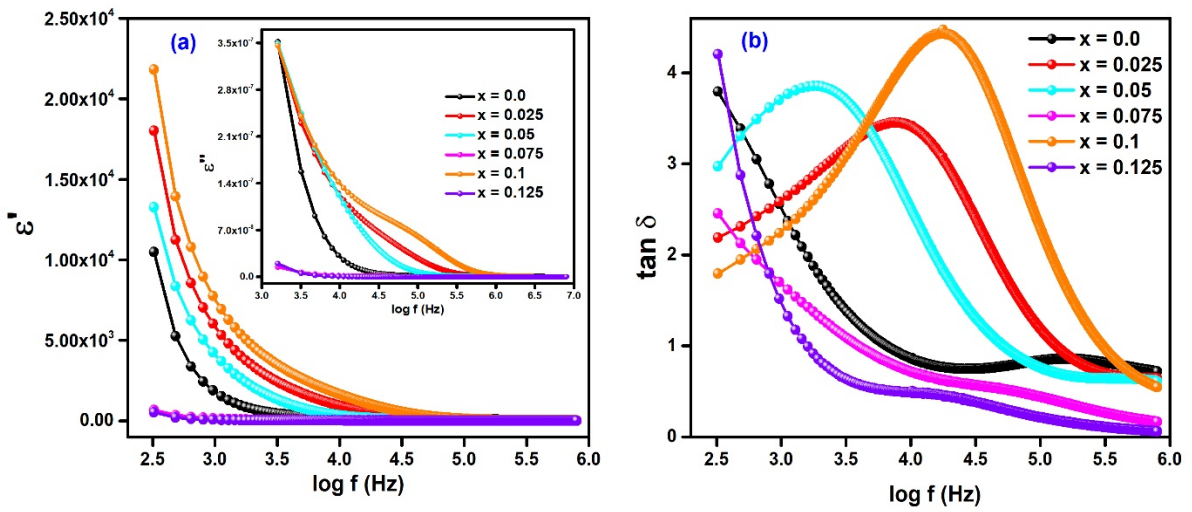


Fig. 16.  $\log f$  versus (a) dielectric constant and loss for La<sup>3+</sup> doped Zn-Co ferrites (b) tangent loss for La<sup>3+</sup> doped ZC nano ferrites

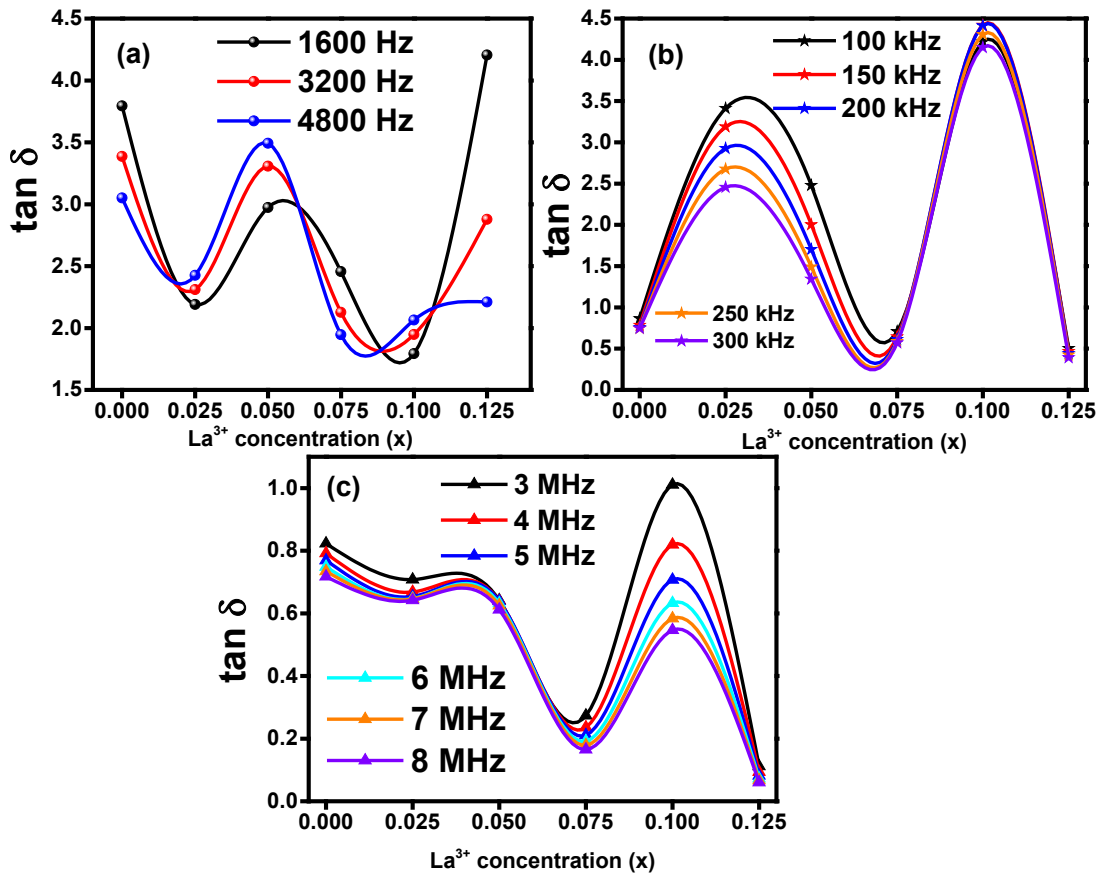


Fig. 17. La<sup>3+</sup> concentration vs tangent loss at different frequencies

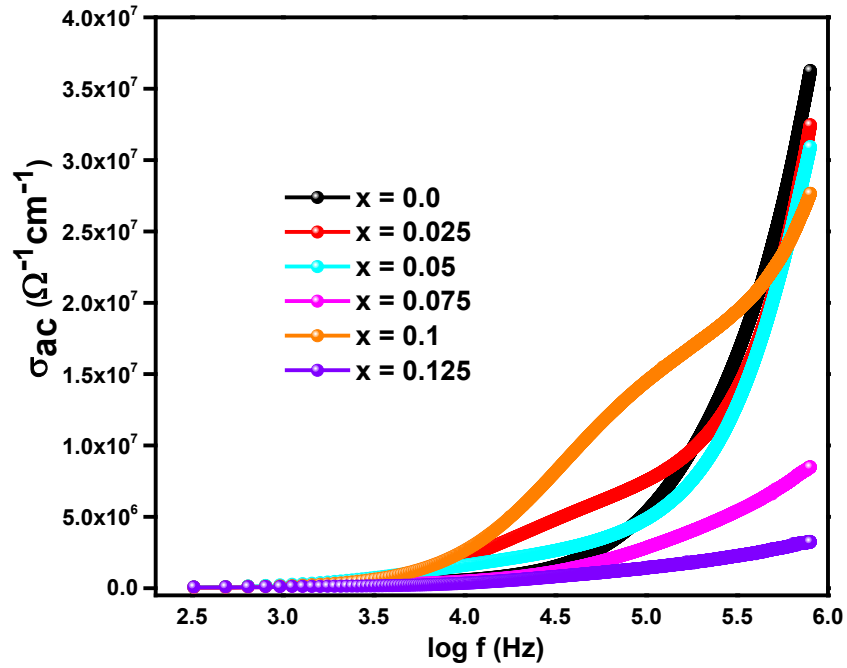


Fig. 18. The plot of log f vs ac conductivity of nano ferrite samples

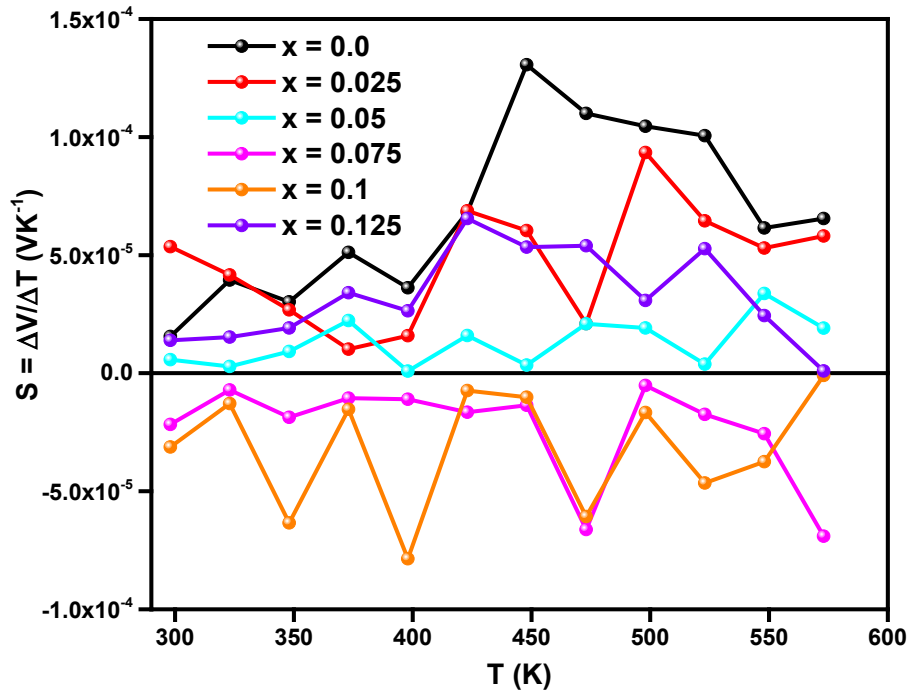


Fig. 19. The variation between temperature and Seebeck voltage coefficient

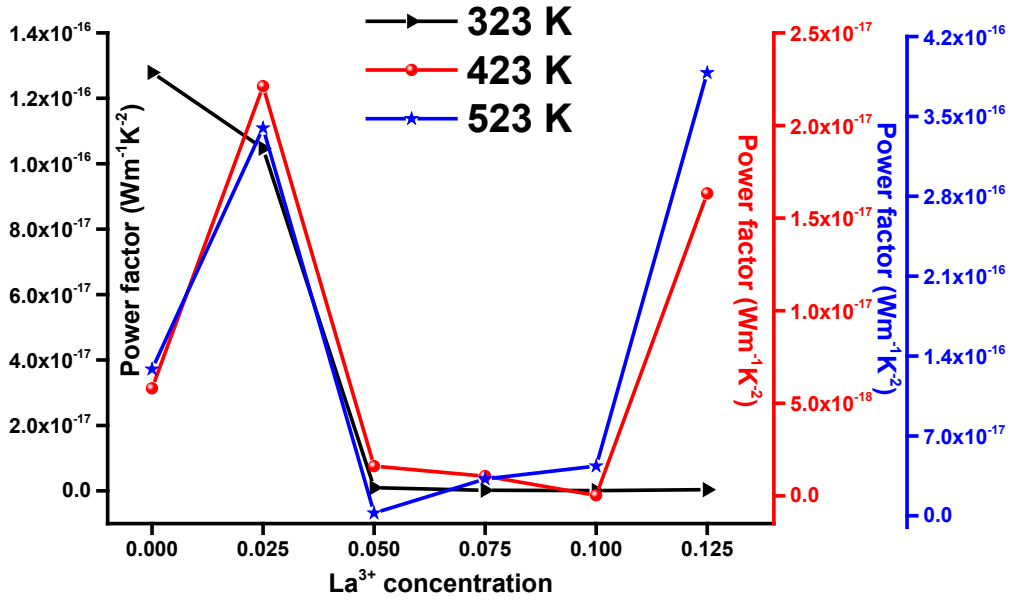


Fig. 20. The plot of  $\text{La}^{3+}$  concentration vs power factor at different temperatures

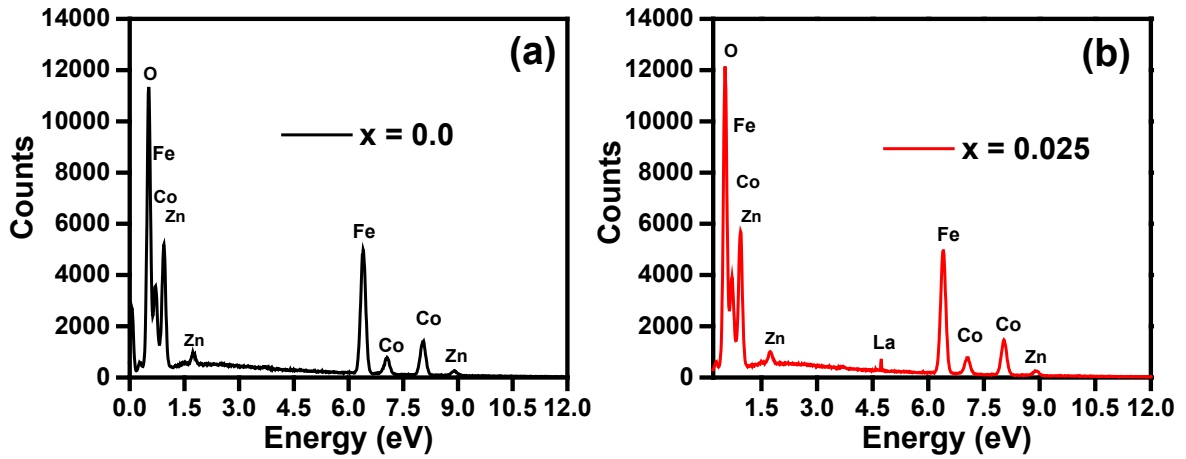


Fig. 21. EDX pattern for  $x = 0.0$  and  $x = 0.025$

**Table 1:**  $\text{La}^{3+}$  concentration ( $x$ ), crystalline size ( $D$ ), interplanar spacing ( $d$ ), the experimental lattice constant ( $a_{\text{exp}}$ ), dislocation line density ( $\delta$ ), unit cell volume ( $V$ ), hopping length  $H_A$ , and  $H_B$  for La-doped ZC nano ferrites powder

$x$	$D \pm 0.1$ (nm)	$d$ (Å)	$a_{\text{exp}}$ (Å)	$\delta \times 10^{-4}$ (nm <sup>-2</sup> )	$V$ (Å) <sup>3</sup>	$H_A$ (Å)	$H_B$ (Å)
0.000	33.6	2.5299	8.3909±0.0042	8.86	590.78	3.6332	2.9661
0.025	20.1	2.5302	8.3919±0.0042	25.0	591.00	3.6337	2.9665
0.050	18.7	2.5320	8.3978±0.0042	28.4	592.24	3.6362	2.9686
0.075	18.4	2.5321	8.3980±0.0042	29.3	592.29	3.6363	2.9687
0.100	17.8	2.5324	8.3990±0.0042	31.4	592.51	3.6368	2.9690
0.125	17.5	2.5325	8.3994±0.0042	31.8	592.58	3.6369	2.9692

**Table 2:** Molecular weight ( $M$ ), X-ray ( $\rho_x$ ), bulk ( $\rho_B$ ) and relative ( $\rho_R$ ) densities, porosity ( $P$ ) percentage, packing factor ( $p$ ), strain ( $\varepsilon$ ), specific surface area ( $S$ ), and polaron radius ( $\gamma_p$ ) for nano ferrites samples

$x$	$M$ (g/mol)	$\rho_x \pm 0.01$ (g/cm <sup>3</sup> )	$\rho_B$ (g/cm <sup>3</sup> )	$\rho_R$ (%)	$P$ (%)	$p$	$\varepsilon$	$S$ (cm <sup>2</sup> /g)	$\gamma_p$ (Å)
0.000	237.79	5.34	3.29	162.57	38.38	132.77	0.0035	0.0333	0.7514
0.025	239.86	5.39	3.39	159.09	37.10	79.11	0.0059	0.0555	0.7515
0.050	241.93	5.42	3.89	139.55	28.22	74.14	0.0063	0.0588	0.7520
0.075	244.01	5.47	4.48	122.20	18.09	73.00	0.0064	0.0592	0.7520
0.100	246.09	5.51	4.71	117.18	14.51	70.43	0.0066	0.0609	0.7521
0.125	248.17	5.56	4.95	112.43	11.05	69.98	0.0067	0.0608	0.7522

**Table 3:** Theoretical structural parameters for as-prepared samples

$x$	$r_A$ (Å)	$r_B$ (Å)	$a_{th}$ (Å)	$U$ (Å)	$T$	$R_A$ (Å)	$R_B$ (Å)	$R_x$ (Å)	$R_{x'}$ (Å)	$R_{x''}$ (Å)
0.000	0.637	0.652	8.2816	0.3866	1.0499	1.9852	2.0004	3.2418	2.6914	2.9730
0.025	0.637	0.657	8.2951	0.3863	1.0484	1.9822	2.0025	3.2370	2.6969	2.9731
0.050	0.637	0.663	8.3109	0.3861	1.0467	1.9798	2.0061	3.2330	2.7051	2.9749
0.075	0.637	0.672	8.3249	0.3857	1.0441	1.9741	2.0094	3.2237	2.7144	2.9746
0.100	0.637	0.677	8.3399	0.3854	1.0425	1.9708	2.0117	3.2184	2.7205	2.9747
0.125	0.637	0.683	8.3543	0.3852	1.0410	1.9675	2.0138	3.2130	2.7262	2.9746

**Table 4:** Interionic distance between the ions for all the samples

$x$	$p$ (Å)	$q$ (Å)	$r$ (Å)	$s$ (Å)	$b$ (Å)	$c$ (Å)	$d$ (Å)	$e$ (Å)	$f$ (Å)
0.000	2.0004	1.9852	3.8013	3.6895	2.9666	3.4786	3.6333	5.4500	5.1383
0.025	2.0025	1.9822	3.7957	3.6889	2.9669	3.4791	3.6338	5.4507	5.1389
0.050	2.0061	1.9798	3.7910	3.6902	2.9690	3.4815	3.6363	5.4545	5.1425
0.075	2.0094	1.9741	3.7802	3.6884	2.9691	3.4816	3.6364	5.4546	5.1427
0.100	2.0117	1.9708	3.7739	3.6876	2.9694	3.4820	3.6368	5.4553	5.1433
0.125	2.0138	1.9675	3.7675	3.6867	2.9696	3.4822	3.6370	5.4555	5.1435

**Table 5:** Calculated values of bond angles for La-doped Zn-Co nano ferrites samples

$x$	$\theta_1$	$\theta_2$	$\theta_3$	$\theta_4$	$\theta_5$
0.000	121.57	137.71	95.71	126.53	69.88
0.025	121.64	137.97	95.60	126.51	70.05
0.050	121.72	138.28	95.46	126.48	70.26
0.075	121.84	138.76	95.25	126.44	70.57
0.100	121.92	139.06	95.12	126.41	70.76
0.125	121.99	139.35	95.01	126.38	70.95

**Table 6:** Absorption bands of as-prepared samples

$x$	$\nu_1$ (cm <sup>-1</sup> )	$\nu_2$ (cm <sup>-1</sup> )
0.000	542.32	408.03
0.025	543.46	408.18
0.050	544.18	410.43
0.075	545.67	408.33
0.100	555.69	416.63
0.125	543.88	417.17

**Table 7:** At room temperature Raman modes for La<sup>3+</sup> doped ZC samples

$x$	Raman shift (cm <sup>-1</sup> )				
	$T_{2g}$ (1)	$E_g$	$T_{2g}$ (2)	$T_{2g}$ (3)	$A_{1g}$
0.000	299.35	345.56	464.86	526.95	638.25
0.025	300.16	344.02	466.53	521.62	635.38
0.050	299.45	342.34	463.79	509.93	633.81
0.075	299.11	340.71	462.49	507.72	635.60
0.100	295.39	336.66	465.85	527.86	635.12
0.125	289.99	330.59	464.78	523.08	640.83

**Table 8:** Values of La<sup>3+</sup> concentration, resistivity, activation energy, Curie temperature, drift mobility, and optical bandgap for La<sup>3+</sup> substituted Zn-Co nano-ferrites

$x$	$\rho$ at 313 K $\times 10^8$ ( $\Omega$ cm)	$\Delta E$ (eV)	$T_C$ (K)	$\mu_d \times 10^{-20}$ at 313 K (cm <sup>2</sup> V <sup>-1</sup> s <sup>-1</sup> )	$E_g$ (eV)
0.000	0.0700 $\pm$ 0.0035	1.1686 $\pm$ 0.0058	421	1.7857 $\pm$ 0.0089	1.44
0.025	0.0985 $\pm$ 0.0049	1.1364 $\pm$ 0.0056	383	1.2583 $\pm$ 0.0063	3.17
0.050	0.0294 $\pm$ 0.0015	1.1042 $\pm$ 0.0055	392	3.7479 $\pm$ 0.0187	2.91
0.075	1.7978 $\pm$ 0.0899	1.2233 $\pm$ 0.0061	362	0.0544 $\pm$ 0.0003	3.30
0.100	4.9919 $\pm$ 0.2496	1.7345 $\pm$ 0.0086	352	0.0195 $\pm$ 0.0001	3.63
0.125	4.1843 $\pm$ 0.2092	1.3125 $\pm$ 0.0065	357	0.0221 $\pm$ 0.0001	3.45

**Table 9:** Elemental composition for La<sup>3+</sup> substituted Zn-Co nano-ferrites

<b>Samples</b>	<b>Elements present (mol)</b>				
	<b>Zn</b>	<b>Co</b>	<b>La</b>	<b>Fe</b>	<b>O</b>
<i>Zn<sub>0.5</sub>Co<sub>0.5</sub>Fe<sub>2</sub>O<sub>4</sub></i>	7.43	6.67	-	30.67	55.23
<i>Zn<sub>0.5</sub>Co<sub>0.5</sub>La<sub>0.025</sub>Fe<sub>1.975</sub>O<sub>4</sub></i>	7.13	6.50	0.06	29.57	56.74
<i>Zn<sub>0.5</sub>Co<sub>0.5</sub>La<sub>0.05</sub>Fe<sub>1.95</sub>O<sub>4</sub></i>	7.94	6.20	0.69	28.86	56.31
<i>Zn<sub>0.5</sub>Co<sub>0.5</sub>La<sub>0.075</sub>Fe<sub>1.925</sub>O<sub>4</sub></i>	8.37	7.78	0.94	24.75	58.16
<i>Zn<sub>0.5</sub>Co<sub>0.5</sub>La<sub>0.1</sub>Fe<sub>1.9</sub>O<sub>4</sub></i>	8.94	7.37	1.07	25.23	57.39
<i>Zn<sub>0.5</sub>Co<sub>0.5</sub>La<sub>0.125</sub>Fe<sub>1.875</sub>O<sub>4</sub></i>	8.70	6.47	1.11	24.17	59.55